

EXPERIMENTAL STUDY OF HYBRID COOLED HEAT
EXCHANGER

By

Han-Chuan Tsao

Thesis submitted to the Faculty of the Graduate School of the
University of Maryland, College park, in partial fulfillment
of the requirements for the degree of
Master of Science
2011

Advisory Committee:
Professor Reinhard Radermacher, Chair
Professor Gregory Jackson
Professor James Duncan

© Copyright by

Han-Chuan Tsao

2011

Acknowledgements

My most sincere thanks go to my advisor, the defense committee chair, Dr. Reinhard Radermacher for all of his support. Dr. Radermacher gave me the opportunity to join CEEE two years ago as a graduate assistant, which allowed me to have a comprehensive understanding of energy engineering and conduct this thesis research. His guidance and encouragements have supported and helped me throughout my graduate education, academically, and personally.

I would like to thank the associate director of CEEE, Dr. Yunho Hwang, who has directed me on the research. His insight on how to approach problems has taught me much.

My thanks go to my committee members, Dr. Gregory Jackson and Dr. James Duncan. I appreciate both of them of being in the committee. Their perspectives of the research truly inspired me.

I would like to thank Jan Muehlbauer, whose hands-on approach to problem solving has helped me over many research hurdles. Working with him had been a great learning experience.

To all of my colleagues at the CEEE, I thank all of your helps, supports and friendships. The numerous discussions between us have broadened my knowledge, technically, and culturally.

Finally, I would like to thank my family and friends who have supported me during my studyabroad life. Especially for my grandparents and parents, with your unlimited encouragements and love, I have confidence to pursue the M.S. degree and complete the research.

Table of Contents

Acknowledgements.....	ii
List of Tables.....	vii
List of Figures.....	viii
Nomenclature.....	xi
1. Introduction.....	1
2. Literature Reviews.....	2
3. Project Objectives.....	7
4. Test Facility Design.....	9
4.1 The Design Requirements.....	9
4.2 Test Facility Schematic.....	10
4.3 Air Side Duct Design.....	12
4.3.1 Test Section Design.....	12
4.3.2 Wind Tunnel Design.....	15
4.3.3 Air Side Component Selection.....	16
4.4 Wetting Water Loop Design.....	25
4.4.1 Wetting Water Loop.....	25

4.4.2	Wetting Water Loop Component Selection.....	27
4.5	Heat Exchanger Hot Water Loop Design.....	29
4.5.1	Hot Water Loop Design	29
4.5.2	Hot Water Loop Component Selection	32
5.	Test Facility Construction.....	39
5.1	Air Duct Construction.....	40
5.2	Wetting Water Loop Construction.....	45
5.3	Heat Exchanger Hot Water Loop Construction	47
6.	Experimental Work	50
6.1	Instrument Calibration	50
6.1.1	Humidity Sensor Calibration	50
6.1.2	Air Nozzle Calibration	54
6.1.3	Water Flow Meter Calibration.	64
6.1.3.1	Hot Water Flow Meter Calibration	65
6.1.3.2	Wetting Water Flow Meter Calibration.....	66
6.1.4	Temperature Sensor Calibration.....	67
6.2	Baseline Test Matrix	72

6.3 Uncertainty Analysis	73
6.4 Results and Discussions	77
6.4.1 Dry Condition Test Results	78
6.4.2 Wet Condition Test Results	82
6.4.3 Comparisons and Discussions.....	85
7. Summary and Conclusions	91
8. Recommendations and Future Work.....	95
References:.....	96

List of Tables

Table 1: Air Side Pressure Drop.....	22
Table 2: DP Sensors Specifications	24
Table 3: Water Flow Meter for Wetting Water Loop	27
Table 4: Hot Water Loop Flow Meter	34
Table 5: Compressor Data Sheet [19]	35
Table 6: Tube-Fin HX Detailed Specifications	37
Table 7: Greenspan's Calibration Table [21].....	51
Table 8: Nozzle Calibration: AFR of Single Nozzle.....	59
Table 9: Nozzle Calibration: Discharge Coefficient of Single Nozzle	61
Table 10: Nozzle Calibration: AFR of Two Nozzles	62
Table 11: Nozzle Calibration: Discharge Coefficient of Two Nozzles	63
Table 12: Baseline Test Matrix	73
Table 13: Specifications of Instruments.....	74
Table 14: Uncertainties at Typical Variable Values.....	77
Table 15: Test Result of Dry Cases	81
Table 16: Test Result of Wet Cases	84

List of Figures

Figure 1: Test Facility Schematic	11
Figure 2: The Heat Exchanger Module.....	12
Figure 3: The Test Section with Heat Exchanger.....	13
Figure 4: The Heat Exchanger Slide-in Procedure	14
Figure 5: The 45° and 90° Inclination Angle of the Heat Exchanger.....	15
Figure 6: Test Facility Design Overview	15
Figure 7: ASHRAE Standard Wind Tunnel Chamber [15].....	16
Figure 8: ASHRAE Standard Heat Exchanger Chamber [15].....	16
Figure 9: 5-Inch (0.13 m) Air Nozzle Grid	19
Figure 10: Axial Air Fan	23
Figure 11: AB16 Air Mixer.....	24
Figure 12: NESLAB HX500 Chiller.....	25
Figure 13: Wetting Water Loop.....	26
Figure 14: Water Pump for Wetting Water Loop	28
Figure 15: Water Pump Curve for Wetting Water Loop [17].....	29
Figure 16: HX Hot Water Loop	31
Figure 17: HP75 Pump Curve [18]	33
Figure 18: Selected Sporlan TXV	36

Figure 19: Tube-fin HX	37
Figure 20: Hot Gas Bypass Valve	38
Figure 21: The Overview of the Test Facility	39
Figure 22: The Existing Air Duct in CEEE Lab.	40
Figure 23: Rearrangement of the Air Duct	41
Figure 24: Modified Test Facility	41
Figure 25: Modified Dimension of the Test Facility.....	42
Figure 26: Air Mixer and Flow Settling Means	43
Figure 27: Air Flow Settling Means and Air Nozzles.....	43
Figure 28: Air Mixer, RH sensor and TC Grid	44
Figure 29: RH Sensor, TC Grid and Air Flow Settling Means	44
Figure 30: Axial Fan Installation	45
Figure 31: The Chiller.....	45
Figure 32: Wetting Water Side Plate HX	46
Figure 33: Wetting Water Distributor.....	47
Figure 34: The Hot Water Loop Plate HX	48
Figure 35: Secondary Refrigerant Loop	48
Figure 36: Water Loops Charge System	49
Figure 37: Humidity Sensor Calibrator.....	52

Figure 38: Calibration Result of RH Sensor #1	53
Figure 39: Calibration Result of RH Sensor #2	53
Figure 40: ASHRAE Standard Nozzle [15]	54
Figure 41: Air Nozzle Calibration Chamber [15]	56
Figure 42: Electrical Air Heaters	57
Figure 43: Wattage Meters	57
Figure 44: Nozzle Calibration: AFR of Single Nozzle	60
Figure 45: Nozzle Calibration: Discharge Coefficient of Single Nozzle.....	61
Figure 46: Nozzle Calibration: AFR of Two Nozzles	63
Figure 47: Nozzle Calibration: Discharge Coefficient of Two Nozzles	64
Figure 48: Water Flow Meter Calibration Set-up	65
Figure 49: Hot Water Flow Meter Calibration	66
Figure 50: Wetting Water Flow Meter Calibration	67
Figure 51: Thermocouples Calibration Set-up.....	68
Figure 52: Air Side Inlet Thermocouples Calibration.....	70
Figure 53: Air Side Outlet Thermocouples Calibration	71
Figure 54: Overall Heat Exchanger Capacity Comparison.....	87
Figure 55: Overall Air Side Pressure Drop Comparison	88
Figure 56: Overall Air Fan Pumping Power Comparison.....	89

Nomenclature

Acronyms:

AFR	Air Flow Rate
ASHRAE	American Society of Heating, Refrigerating and Air Conditioning Engineers
CEEE	Center for Environmental Energy Engineering
CFD	Computational Fluid Dynamics
CFM	Cubic Feet per Minute
COP	Coefficient of Performance
DP	Differential pressure
GPM	Gallon per Minute
HVAC	Heating, Ventilation, Air-Conditioning
HX	Heat Exchanger
RH	Relative Humidity
RMS	Root mean squared
RTD	Resistance Temperature Detector
SG	Specific Gravity
TC	Thermocouple
TXV	Thermostatic Expansion Valve

Abbreviations:

A	Area [m ²]
C	Discharge Coefficient
C _p	Specific Heat [kJ/kg-K]
C _v	Flow Coefficient
D	Diameter [m]
E	Energy [kWh]
F	Fluid Volume Flow Rate [GPM]
h	Enthalpy [kJ/kg]
m	Mass [kg]
P	Pressure [Pa]
Q	Air Flow Rate [m ³ /s]
q	Capacity [W]
R	Coefficient of Determination
Re	Reynolds Number
T	Temperature [°C]
u	Uncertainty
v	Velocity [m/s]
Y	Expansion Factor

α	Ratio of Nozzle Throat Pressure to Nozzle Entrance Pressure
β	Ratio of Nozzle Throat Diameter to Air Duct Diameter
ρ	Density [kg/m ³]
η	Energy Balance [%]
ΔP	Pressure Difference [Pa]

Subscripts:

a	Air
act	Actual
adj	Adjusted
d	Air Duct
h	Heater
i	Inlet
id	Ideal
n	Nozzle
o	Outlet
v	Vapor
w	Water
ww	Wetting Water

1. Introduction

The technique of evaporative cooling, including spray cooling and deluge cooling, is highly and widely applied in heat exchanger applications, such as commercial or residential HVAC systems. Therefore, the issue of evaporative cooling heat transfer enhancement on heat exchangers is very worthy of further research. The first step of heat exchanger evaporative cooling research was to have an overall understanding of the airside performance of the heat exchanger. Meanwhile, the water retention mechanism plays an important role in the present work, and it also has significant effects on the performance of heat exchangers. However, the retained water characteristics highly depend on the wettability of the heat exchanger surface [1], so it is necessary to clarify the influences and significances of wettability. This research will design and build a test system for investigating the performance of an air-cooled round-tube-fin heat exchanger under different test conditions in order to develop a qualitative and quantitative understanding of air side heat transfer and pressure drop enhancement. The goal of this project will be the development of an experimental method to research the heat exchanger performance under both dry and wet conditions. A fundamental experimental work will be introduced and conducted. The baseline test matrix will include several factors that will be varied in a reasonable range.

2. Literature Reviews

Evaporative cooling for heat exchangers can enhance heat transfer performance. For a spray cooling application, Yang and Clark [2] did an experimental research for the air side performance of three different fin types of heat exchangers: plain-fin, louvered-fin and perforated-fin. They indicated that the spray cooling could enhance the overall heat transfer coefficient by 40% at a low Reynolds number ($Re=500$) for all types of heat exchangers. However, at high Reynolds number ($Re=7000$) it was only enhanced by 12.7%, 6.1% and 12.5% for plain-fin, louvered-fin and perforated-fin, respectively. Leidenfrost and Korenic [3] developed an analytical model to investigate the air side spray cooling enhancement performance of a plain-fin-tube heat exchanger under dry and wet conditions. They indicated that the performance of condensers could be enhanced significantly by evaporative cooling. They introduced the coefficient of enhancement K_e , which was defined as the ratio of heat loads of wetted to dry condensers. In their 40 cases, inlet air flow velocity varied from 1 m/s to 10 m/s, and relative humidity varied from 50% to 100%: the highest K_e can reach 5.58 when velocity is 1 m/s and RH is 50%, and the lowest K_e is 2.57 when velocity is 10 m/s and RH is 100%. It showed that evaporative condensers could be used very beneficially. For modern applications, a louvered-fin-flat-tube is widely used in heat exchangers. Song et al. [4] investigated a 2-D model for a louvered fin

heat exchanger and assumed the surface of the heat exchanger is fully covered with a thin water film. Their results showed that cooling performance can be increased up to four times greater than the baseline performance by applying the evaporative cooling. However, the increment highly depends on the fin parameters, Bi and κ . Bi is defined as a function of ambient air heat transfer coefficient, heat transfer surface, fin height, and effective fin conductivity, and κ is defined as the ratio of effective air conductivity to effective fin conductivity. Hence, Bi and κ are dependent on the fin thickness; in other words, fin thickness played an important role in their model of predicting air side cooling enhancement performance. When the fin is not sufficiently thick, the cooling enhancement by the evaporative cooling decreases. However, there were some research groups that showed that the wet surface of a heat exchanger could not enhance the heat transfer performance. Wang et al. [5] compared the air side performance between several different fin-and-tube heat exchangers with varying geometry. They tested the performance under both dry and wet conditions and applied the hydrophilic coating to investigate the effect of the coating on the heat exchanger performance. They found out that the airside heat transfer coefficient was reduced by 20% by applying the hydrophilic coating, while the air side pressure drop was reduced by 40%. These results conflicted with the previous research.

Instead of doing research analytically, many researchers have attempted to develop experimental correlations to predict the air side performance, including heat transfer coefficient and pressure drop. However, the correlations for air side thermal hydraulic performance under wet conditions are still limited, especially for louvered-fin-flat-tube heat exchangers. Wang et al. [6] designed an experiment for 10 louvered-fin-round-tube heat exchangers and developed correlations of heat, momentum and mass transfer. They claimed that their results can correlate the present database with a mean deviation of 5.94%, 6.1% and 7.89%, respectively. Kim et al. [7] well integrated previous papers and research into a review paper, which showed several correlations for louvered-fin-flat-tube under dry conditions, but correlations were limited for wet conditions. All the correlations were listed in a comprehensive table. Kim and Bullard [8,9] and Park and Jacobi [10,11] were the only two research groups that published their correlations to predict the air side performance of a louvered-fin-flat-tube under wet conditions based on Chang and Wang's research for louvered-fin-flat-tubes under dry conditions [12]. Kim and Bullard [8, 9] did an experimental study by changing the louvered-fin-flat-tube heat exchanger's geometric parameters: flow depth, fin pitch, tube pitch, number of louvers, and louver angle. Next, they developed correlations to predict friction factor f and Colburn J-factor based on the Reynolds number and geometric parameters. Park and Jacobi [11]

integrated previous studies and their own heat exchanger data into a combined database. A brand-new concept was introduced by Park and Jacobi, in which they developed correlations of j and f factors in terms of wet-surface multipliers ϕ . Wet-surface multipliers are the ratio of wet-surface j and f factors to dry-surface j and f factors. Based on convincing dry-surface experimental results or correlations, wet-surface j and f factors can be obtained with RMS (root mean square) errors of 21.1% for j and 24.4% for f factors. If accurate dry-surface information is unavailable, Park and Jacobi also developed stand-alone j and f factors, which can predict j and f data with RMS errors of 22.7% and 29.1%, respectively. They claimed that the advantage of using wet-surface multipliers instead of independent wet j and f factors with experimental uncertainties, unidentified errors, and inconsistent data reduction method, is the ability to reduce biases from systematic errors in the individual experiments and inconsistent data interpretation methods [11].

A few groups did research and then used the resulting data to develop correlations and predictions about heat and mass transfer performance under wet conditions [8-12].

However, their works focused on water condensate on cold surfaces, meaning the surface temperatures were below the dew points of the experimental conditions and the water condensate would occur spontaneously. However, research about spray cooling or evaporative cooling on heat exchangers, especially for flat-tube-fin type

heat exchangers, is still not quite fully understood. Most of the evaporative cooling research has been focused on single-fin test element surfaces or small-scale applications [13, 14]. Because of the lack of literature, evaporative cooling research methods are not consistent for relatively large applications, such as a core of heat exchangers. Air side performance for a louvered-fin-flat-tube heat exchanger under evaporative cooling conditions needs to be clarified. Although there has been research examining evaporative cooling for louvered-fin-flat-tube heat exchangers, accurate correlations have not been suggested by researchers. A definitive comparison between the various research efforts does not exist. Additionally, there are many correlations to predict air side performance under dry condition, and several papers have indicated correlations for wet conditions. Unfortunately, their work has focused on water condensate problems, which cannot represent the heat and mass transfer performance for evaporative cooling because heat transfer due to evaporation plays an important role on a hot surface. Accordingly, there is a significant research gap that should be filled.

3. Project Objectives

The objective of this project was to measure the performance of an air-cooled outdoor condenser unit under hybrid (air-cooled and evaporatively-cooled) cooling conditions.

The design capacity of the heat exchanger was 17 kW. The research began by brainstorming the various research approaches, and resulted in the design of the test facility for the conventional tube-fin heat exchanger. Eventually, the test facility was built based on the design. The final goal of this thesis was to conduct the shakedown and baseline tests as a basis for future research.

The operating conditions were provided by the project sponsor, and are as follows:

- The ambient air temperature and relative humidity are 22°C and 30%, respectively.
- The heat exchanger frontal air velocity is 1.43 m/s.
- The inlet and outlet temperature of the test heat exchanger are 35°C and 31°C, respectively.
- The heat exchanger water flow rate is 1.01 l/s.
- The wetting water flow rate is 0.16 l/s.
- The heat exchanger inclination angle to the vertical is 20°.

Based on the above information, the test facility was designed to satisfy the requirements. The system should be able to provide a wide range of operating conditions that could cover and exceed the designed operating conditions and specifications. Additionally, the inclination angle of the heat exchanger should be able to be adjusted in the test facility.

4. Test Facility Design

In order to conduct the research successfully, the test facility should be designed well and properly.

4.1 The Design Requirements

There were several requirements that had to be interpreted. First, the dimensions of the test facility needed to be compatible with the dimensions of the environmental chamber. Because there were several components in the system, the layout had to be arranged properly. Second, in order to provide the hot temperature to the test heat exchanger, the hot water loop was used to simulate the refrigerant cycle. Third, the test section needed to be designed such that a $0.5\text{m} \times 0.5\text{m}$ size heat exchanger core could be fitted into the test section. Third, the inclination angle of the heat exchanger needed to be adjustable. Fourth, the heat exchanger should be able to be replaced easily. The idea was to modularize the heat exchanger so the experiment operator could change the heat exchanger without difficulty. Finally, the capacity of the heat exchanger was set to be 17 kW according to the project sponsor; therefore, all the components and equipment of the test facility should be able to satisfy the capacity of the heat exchanger.

Furthermore, the construction material should be selected properly. For recording

purposes, the test section should be constructed from a transparent material such as clear acrylic sheets. The exhaust section of the test facility walls should be well insulated from the surrounding ambient conditions in order to obtain accurate and precise temperature measurements.

4.2 Test Facility Schematic

The test facility schematic is shown in Figure 1. The arrows represent the air-flow direction, which entered the wind tunnel from the left side of the system. After passing through an air-flow settling means, the humidity sensor and temperature measurement grid will record the inlet air condition. The air nozzles grid was made by ASHRAE standard nozzles. Accordingly, once the differential pressure of the nozzles grid was measured, the air volume flow rate could be calculated based on ASHRAE Standard 41.2-1987 [15]. There was one more air-flow straightener located in front of the test section that could ensure that the frontal air-flow of the heat exchanger was uniform. The gap between the heat exchanger and wall was sealed to ensure that all the air-flow would pass through the heat exchanger without any bypass air-flow. The pressure drop of the heat exchanger was also very important to this research. Thus, differential pressure sensors were also installed in front of and behind the heat exchanger. In order to accurately measure the outlet temperature and humidity, the air

mixer and air-flow straighteners, which were mounted in sequence, were essential. Finally, the air-flow exhausts into the ambient surroundings from the top of the exhaust section.

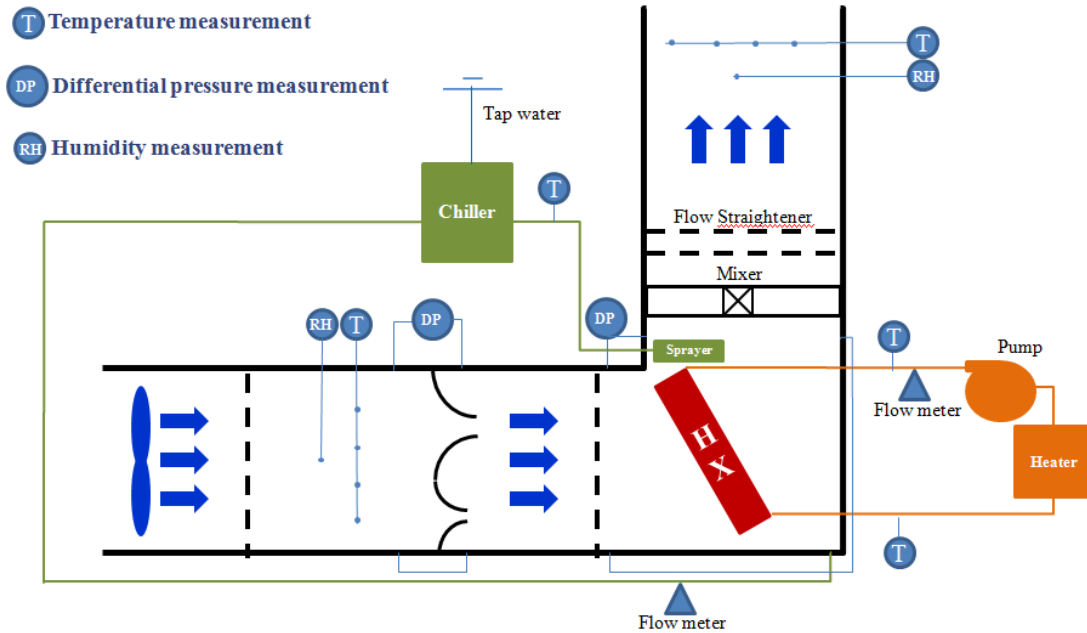


Figure 1: Test Facility Schematic

In addition to the air loop, this system contained two additional water loops: a wetting water loop and a hot water loop. The wetting water loop provided the wetting water to the heat exchanger for either spray cooling or deluging cooling. The hot water loop provided the heat to the heat exchanger to simulate the outdoor condenser unit. The water flow rate and temperature of both the wetting and hot water loops will be controlled and become one of the design variables. The detail designs for each of the air side and water side sections are described in the following sections.

4.3 Air Side Duct Design

There were two major parts for the air duct design. One is the test section design, and the other is the wind tunnel design.

4.3.1 Test Section Design

The test heat exchanger design drawing is shown in Figure 2. The center part of the frame is the heat exchanger core. The plate on the bottom of the frame is called the air-flow guide, and it is designed for guiding the air-flow to the heat exchanger and sealing the heat exchanger between the frame and the drainage slope, which is described in the next section.

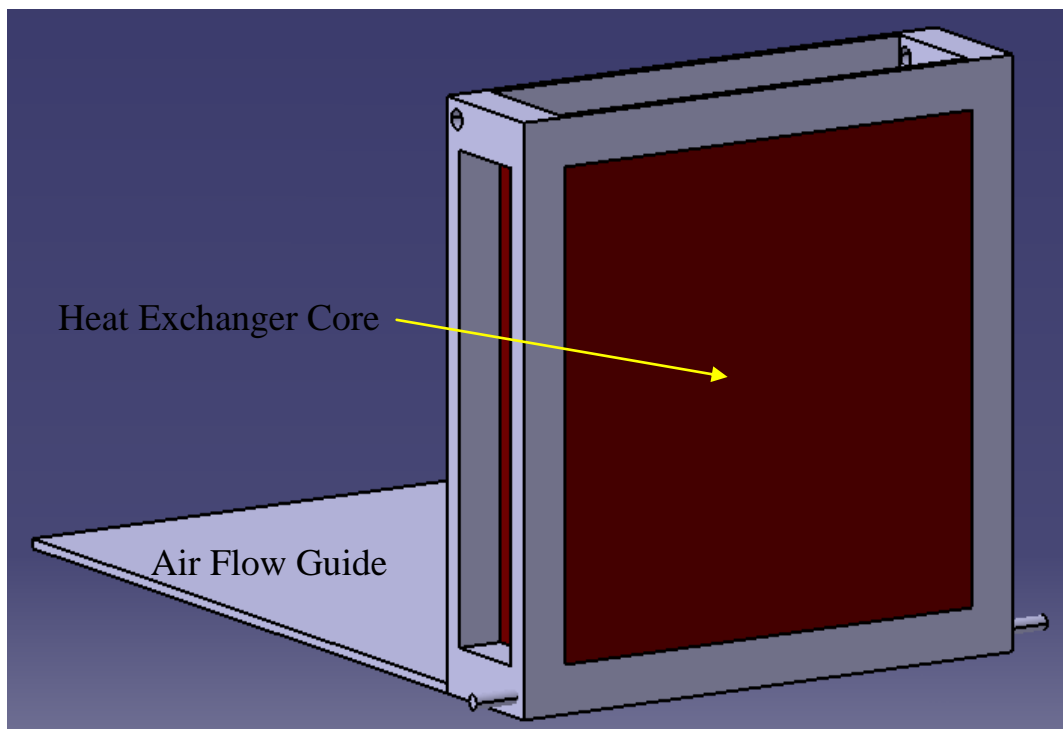


Figure 2: The Heat Exchanger Module

Figure 3 shows the heat exchanger placement within the test section. In this drawing, the basic functions of the test section can be seen. First, the enclosure of the test section was made of transparent material for observing purposes. Second, the tracks on the side walls allowed for changes in the heat exchanger inclination angle. Third, there was a drainage slope on the bottom of the test section, which was designed to collect the drainage from the wetting water when running the system under wet conditions.

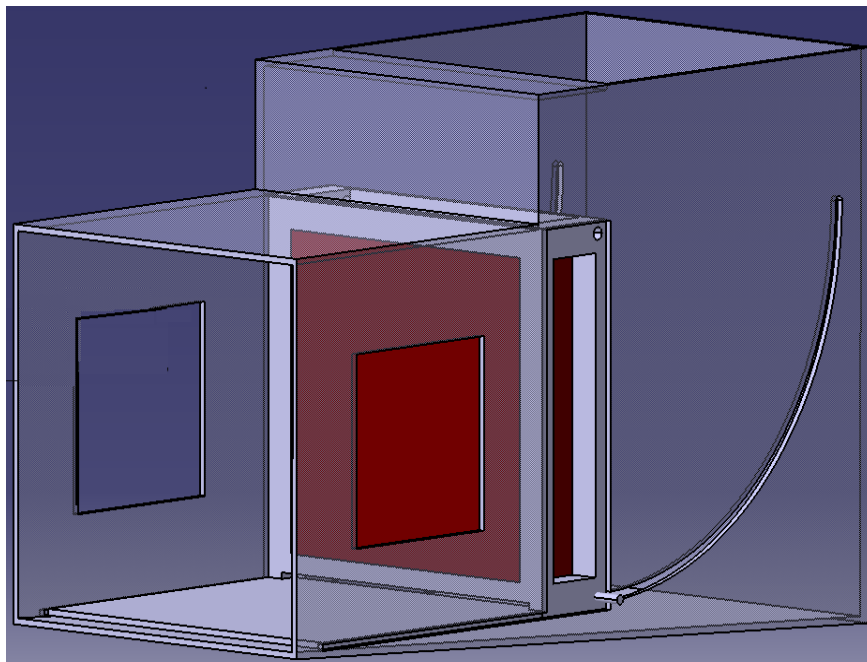


Figure 3: The Test Section with Heat Exchanger

Figure 4 shows the slide-in procedure for installing a heat exchanger into the test section. Once the heat exchanger is completely in place, the experiment operator used the access opening to seal the interior of the air-duct, ensuring that all the air-flow

would pass through the heat exchanger. The tracks behind the heat exchanger allows for adjustments in the inclination angle of the heat exchanger.

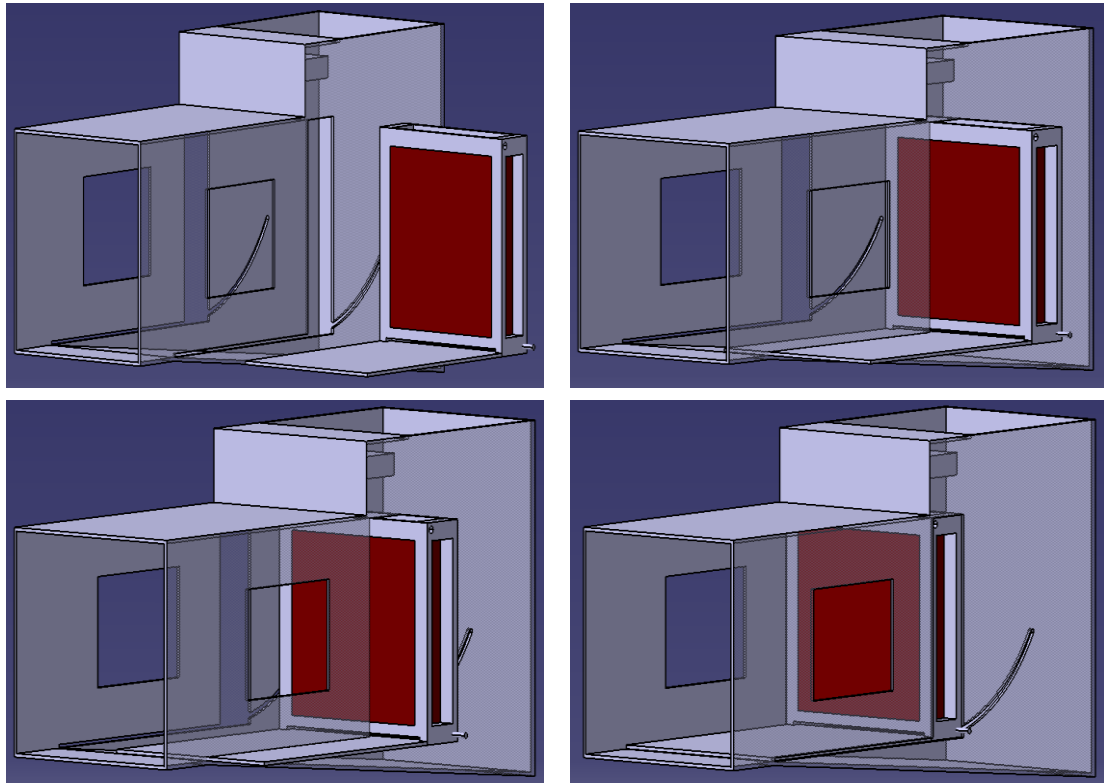


Figure 4: The Heat Exchanger Slide-in Procedure

Figure 5 shows the adjustment of the heat exchanger inclination angle. The heat exchanger simply follows the tracks on the side walls of the test section to adjust to any angle between 0° and 90° . Meanwhile, the angle of the air-flow guide is also adjustable. So that, the air guide could always contact with the bottom wall and avoid the air-flow bypass.

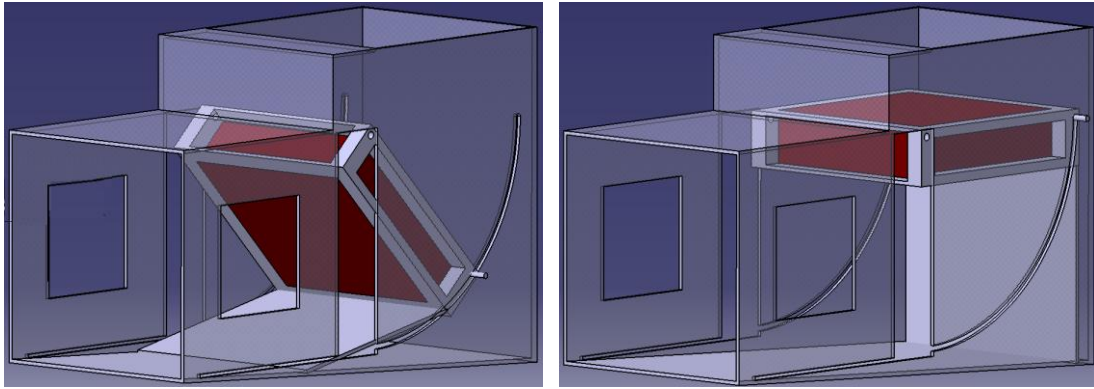


Figure 5: The 45° and 90° Inclination Angle of the Heat Exchanger

Finally, combining all the components and design above, the entire design is shown in

Figure 6.

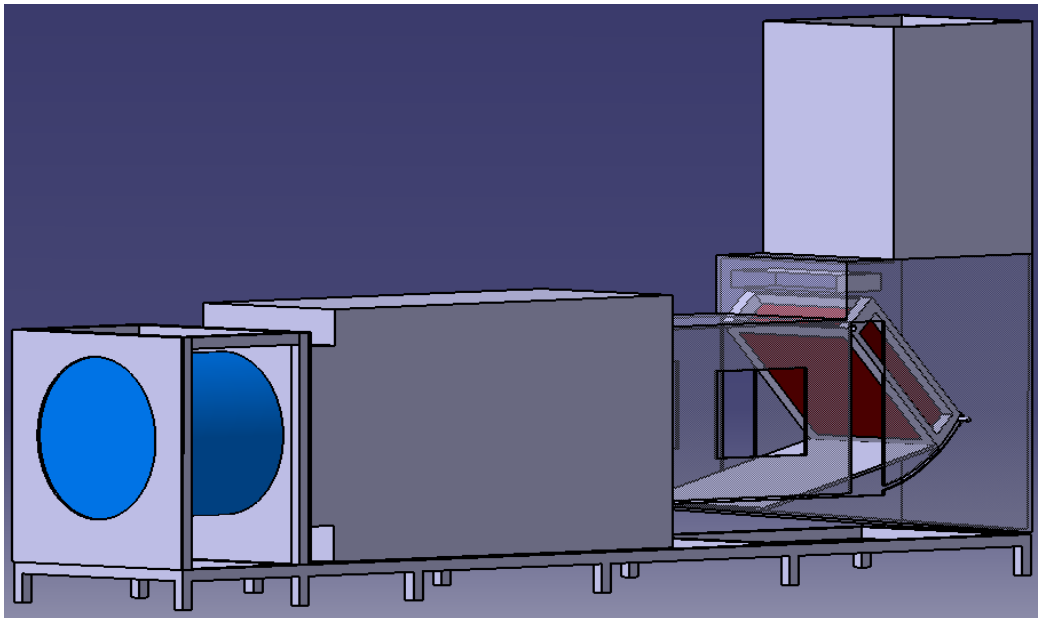


Figure 6: Test Facility Design Overview

4.3.2 Wind Tunnel Design

The wind tunnel chamber was designed and built following ASHRAE Standard 41.2 [15]. Figure 7 and Figure 8 show the dimensions of the wind tunnel and heat exchanger chamber according to the ASHRAE Standard 41.2 [15]. In these drawings,

the M represents the hydraulic diameter of the air duct, and the settling means work as the same as the air flow straightener. Accordingly, all the dimensions in the air duct will follow these two requirements.

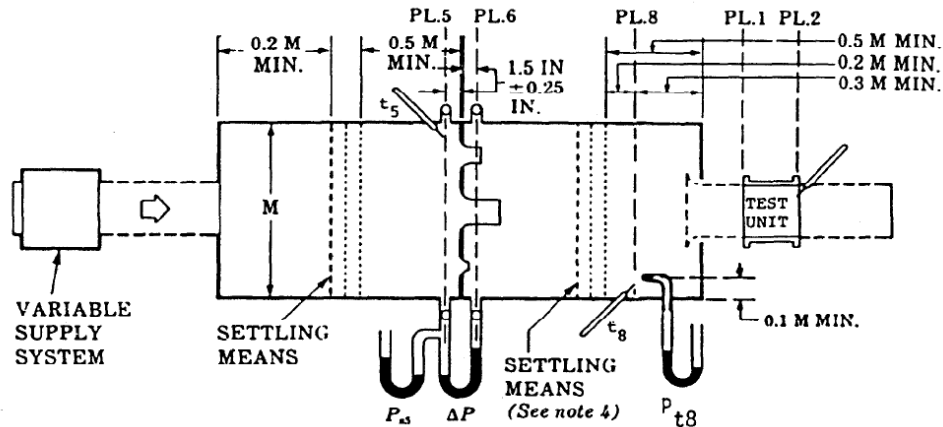


Figure 7: ASHRAE Standard Wind Tunnel Chamber [15]

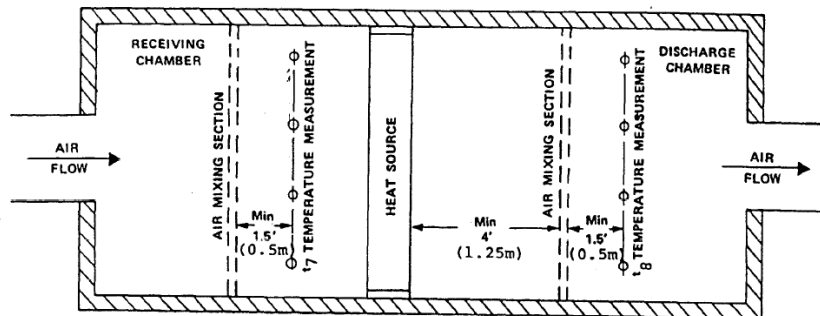


Figure 8: ASHRAE Standard Heat Exchanger Chamber [15]

4.3.3 Air Side Component Selection

There were several components that needed to be selected appropriately. First, an air fan or air blower was the most important component for the air side. The air fan was sized based on the air volume flow rate and air side pressure drop estimation. For the purpose of measuring the rate of the air volume flow, an ASHRAE Standard air

nozzle(s) was needed. The air nozzle(s) was sized based on the targeted heat exchanger frontal air velocity range. To measure the air side pressure difference across the air nozzle grid and heat exchanger, two differential pressure transducers were needed. In order to measure the temperature accurately, an air-flow mixer installed between the test heat exchanger and outlet temperature measurement grid. For all of the component selections, the principle was to use the existing equipment in the Center for Environmental Energy Engineering (CEEE) Laboratory instead of purchasing brand-new components. However, this approach might have resulted in some of the components being oversized for the testing parameters.

4.3.3.1 Air Nozzles Selection

Before sizing the air nozzles, the range of the air volume flow rate should be calculated based on the purposed air velocity range. According to the project requirements, the frontal air velocity was 1.4 m/s when the hybrid cooling was applied. Therefore, the system should be able to provide the velocity of 1.4 m/s. The design parameter for the heat exchanger frontal air velocity had a range of 1 m/s to 3 m/s. This is the typical air velocity of an HVAC outdoor unit. In addition, the designed test heat exchanger frontal area was $0.5 \text{ m} \times 0.5 \text{ m}$, 0.25 m^2 . Therefore, the air volume flow rate was from $0.25 \text{ m}^3/\text{s}$ to $0.75 \text{ m}^3/\text{s}$.

According to the ASHRAE Standard 41.2 [15], the air velocity through the air nozzle

throat should be between 15 m/s and 35 m/s. Therefore, the air nozzles were determined by the following calculation:

First, for the upper limit of the air nozzle throat velocity, 35 m/s, the area of the air nozzle throat was calculated using Equation 1:

$$A_n = \frac{Q}{v_n} = \frac{0.75}{35} = 0.021 \text{ m}^2 \quad \text{Equation 1}$$

However, this air nozzle did not satisfy the ASHRAE Standard [15] because the resulting air nozzle throat velocity, at the air volume rate of $0.25 \text{ m}^3/\text{s}$, was lower than 15 m/s (see Equation 2):

$$v_n = \frac{Q}{A_n} = \frac{0.25}{0.021} = 11.9 \text{ m/s} \quad \text{Equation 2}$$

Second, for the lower limit of the air nozzle throat velocity, 15 m/s, the air nozzle throat area was calculated using Equation 3:

$$A_n = \frac{Q}{v_n} = \frac{0.25}{15} = 0.017 \text{ m}^2 \quad \text{Equation 3}$$

This air nozzle did not satisfy the ASHRAE Standard [15] because of the air nozzle throat velocity, at the air volume rate of $0.75 \text{ m}^3/\text{s}$, was higher than 35 m/s:

$$v_n = \frac{Q}{A_n} = \frac{0.75}{0.017} = 44.1 \text{ m/s} \quad \text{Equation 4}$$

Because one single nozzle could not cover the whole operating range, a multiple air nozzle grid was needed. For this wind tunnel, two 5 inches (0.13 m) ASHRAE Standard nozzles were used to provide sufficient air volume flow and satisfy the ASHRAE Standard 41.2 [15] too. Figure 9 shows the air nozzle grid.



Figure 9: 5-Inch (0.13 m) Air Nozzle Grid

To operate at the low air velocity range, only one nozzle was needed. The following calculation shows the operating range of one nozzle:

$$A_n = 0.013 \text{ m}^2$$

The highest and lowest air-flow rates at an air nozzle throat velocity of 35 m/s and 15 m/s are shown in Equation 5 and Equation 6:

$$Q = A_n \times v_n = 0.013 \text{ m}^2 \times 35 \frac{\text{m}}{\text{s}} = 0.44 \text{ m}^3/\text{s} \quad \text{Equation 5}$$

$$Q = A_n \times v_n = 0.013 \text{ m}^2 \times 15 \frac{\text{m}}{\text{s}} = 0.19 \text{ m}^3/\text{s} \quad \text{Equation 6}$$

The corresponding heat exchanger frontal air velocities were 1.77 m/s and 0.76 m/s, respectively.

To operate at the high air velocity range, two nozzles are needed. The following calculation shows the operating range of two nozzles:

$$A_n = 0.025 \text{ m}^2$$

The highest and lowest air-flow rates at an air nozzle throat velocity of 35 m/s and 15

m/s are shown in Equation 7 and Equation 8:

$$Q = A_n * v_n = 0.025 \text{ m}^2 * 35 \frac{\text{m}}{\text{s}} = 0.89 \text{ m}^3/\text{s} \quad \text{Equation 7}$$

$$Q = A_n * v_n = 0.025 \text{ m}^2 * 15 \frac{\text{m}}{\text{s}} = 0.38 \text{ m}^3/\text{s} \quad \text{Equation 8}$$

The corresponding heat exchanger frontal air velocity was 3.5 m/s and 1.5 m/s, respectively. Accordingly, combining two, 5-inch (0.13 m) nozzles in a grid could cover the air-flow operating range.

4.3.3.2 Air Fan Selection

For selecting the air fan, there were two major factors that needed to be determined: maximum air volume flow rate and air side pressure drop. There are multiple components that can cause a major air side pressure drop: the air nozzles, heat exchangers, the air mixer, air flow settling means, and the air duct itself.

For the maximum air-flow rate, 0.89 m³/s is equal to 1885 CFM. The corresponding pressure drop can be calculated according to Equation 9, to obtain 486.5 Pa:

$$\Delta P = \frac{1}{2} \rho (v_o^2 - v_i^2) \quad \text{Equation 9}$$

According to the manufacturer of the air mixer, the maximum pressure drop was 0.2 w.g.” (water gauge in inch), which is equal to 50 Pa.

According to ASHRAE Standard 41.2-1987 for the air-flow settling means, the mesh sheets installed in the duct must have an open area equal to 50-60% of the total area [15]. Three mesh sheets were installed. The pressure drop across each of them was

estimated to be 80 Pa, so the total pressure drop calculated as 240 Pa.

The fourth source of a drop in air side pressure was the air duct itself. The pressure drop of the air duct can be divided into two parts: major losses due to the change of air duct geometry, and minor losses due to the surface friction. The air duct was assumed to be smooth surface, and the Reynolds number was calculated to be 73,263 based on the known air velocity, air duct size and ambient air properties. Therefore, according to Moody Chart [16], the friction factor is 0.019.

The major and minor losses were calculated based on known properties, and total air duct pressure drop was 9.51 Pa.

The last factor in the air side pressure drop estimation was the test heat exchanger. Having no further information about the sponsor's heat exchanger, the air side pressure drop was estimated at 300 Pa. This was over-estimated for most of the HVAC outdoor condenser unit, but it was a conservative estimation.

The detailed air side pressure drop breakdown is shown in Table 1.

Table 1: Air Side Pressure Drop

Pressure drop sources	Pressure drop (Pa)
Air nozzles	486.5
Air mixer	50
Air settling means	240
Air duct	9.5
Heat exchanger	300
Total	1,086 (4.4 inches water gauge)

An axial fan, Hartzell fan model 52-225TA-STFCL2 (see Figure 10), was available in the CEEE Heat Pump Laboratory. According to the manufacturer's performance sheet, this fan was able to provide a 3,037 CFM (1.42 m³/s) air volume flow rate at the pressure drop of up to 5 inches water gauge (1,234 Pa). Therefore, this fan was appropriate for this project.



Figure 10: Axial Air Fan

4.3.3.3 Differential Pressure Sensors Selection

There were two differential pressure sensors in this system. One was for the air nozzle grid and the other was for measuring the pressure difference across the heat exchanger.

The differential pressure sensor model was selected based on the previously estimated pressure drop for these two components (Table 1). Setra System's differential pressure sensors were used, and the specifications for the sensors are shown in Table 2:

Table 2: DP Sensors Specifications

Specifications	Values
Range	0 to 5 inches w.g. (1,234 Pa)
Accuracy	±1% of full scale
Signal type	4 mA to 20 mA

4.3.3.4 Air Flow Mixer Selection

The air mixer selection was determined based on the air volume rate range. The Model AB16 air mixer was used (Figure 11). The operating range of this air mixer was between 2,700 CFM (1.26 m³/s) and 400 CFM (0.19 m³/s).

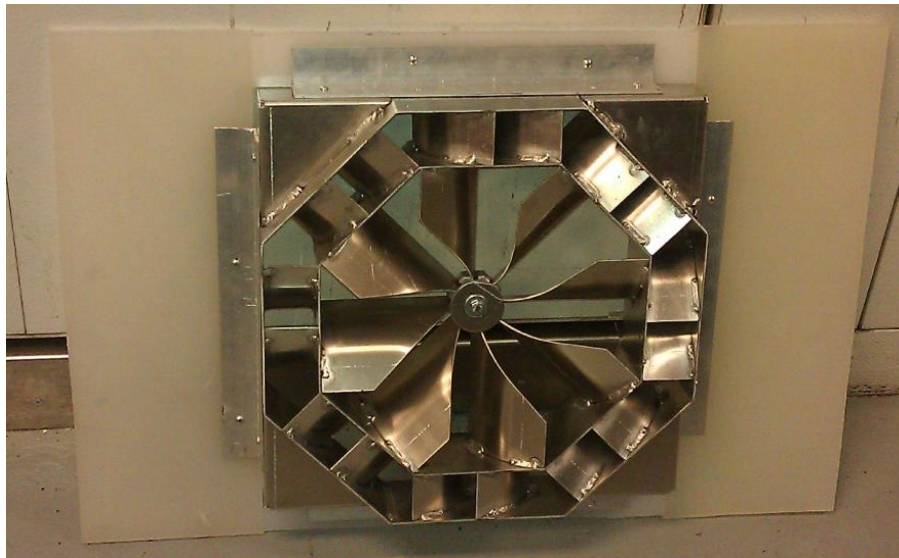


Figure 11: AB16 Air Mixer

4.4 Wetting Water Loop Design

The purpose of the wetting water loop was to control the wetting water conditions to the heat exchanger. Both the temperature and the flow rate have to be controlled well in order to obtain meaningful results.

4.4.1 Wetting Water Loop

The chiller model NESLAB HX-500 was used to maintain the wetting water temperature (Figure 12).



Figure 12: NESLAB HX500 Chiller

The capacity of this chiller was 15 kW. Because it is water cooled, it needed to be connected to the tap water. The water supply's temperature and flow rate were adjusted by using this chiller.

Figure 13 shows the diagram of the wetting water loop. The wetting water loop was an open loop. Therefore, an additional plate type heat exchanger and a water pump needed to be introduced into this loop. This approach allows easy control of the wetting water temperature and water volume flow rate. A water flow meter was installed to record and monitor the water volume flow rate, which was controlled by a ball valve. The temperature measurement of the wetting water inlet was used to record the wetting water for both inlet and outlet temperature. Accordingly, the temperature and flow rate could be controlled properly.

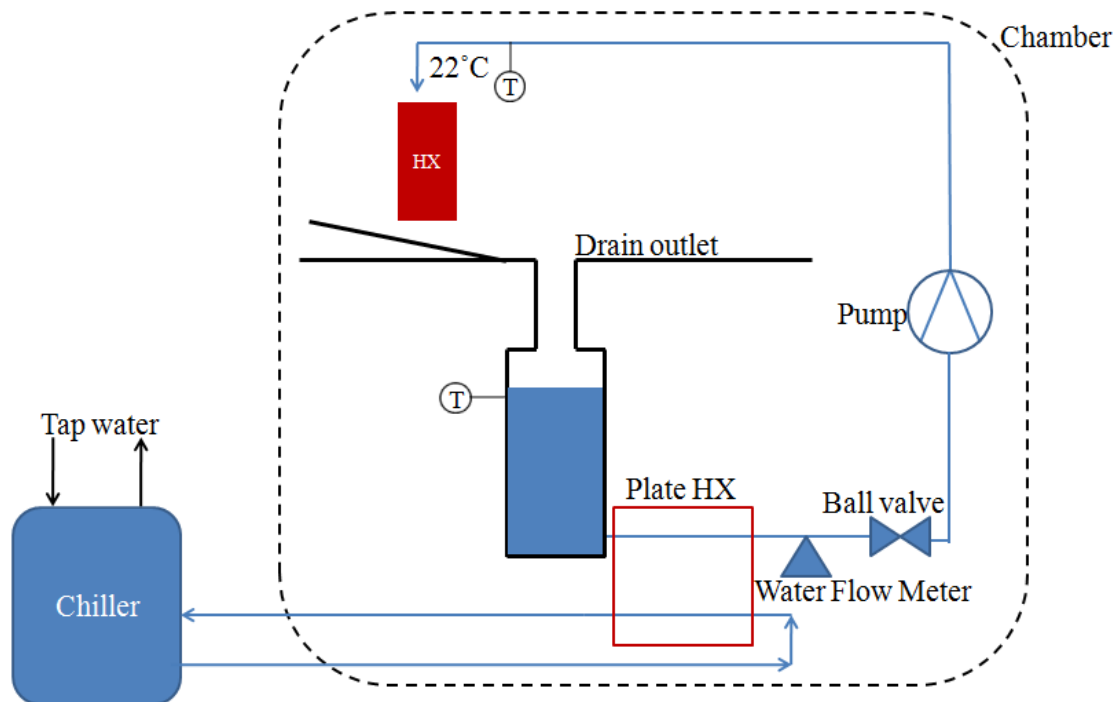


Figure 13: Wetting Water Loop

4.4.2 Wetting Water Loop Component Selection.

Besides the chiller and the ball valve, which already existed in the CEEE Heat Pump Laboratory, the water flow meter, the plate heat exchanger, and the pump needed to be determined.

First, the flow meter specifications needed to cover the proposed operating flow rate condition, which was 0.16 l/s (2.54 GPM). Accordingly, a turbine type water flow meter, Sponsler SP 5/8, was selected. Specifications for the flow meter are shown in Table 3.

Table 3: Water Flow Meter for Wetting Water Loop

Specifications	Values
Water Volume Flow Range	1.75 ~16 GPM (0.11 l/s ~ 1.0 l/s)
Accuracy	±1%

The water pump on the wetting water loop provided the power for re-circulating the wetting water. An Oberdorfer 600 F-13 pump was selected (Figure 14).



Figure 14: Water Pump for Wetting Water Loop

Figure 15 shows the pump curve of the Oberdorfer 600 F-13 pump. The entire pressure drop of the wetting water loop was assumed to be 20 psi (1.38×10^5 Pa).

Therefore, this pump was sufficient to provide the power for re-circulating the wetting water.

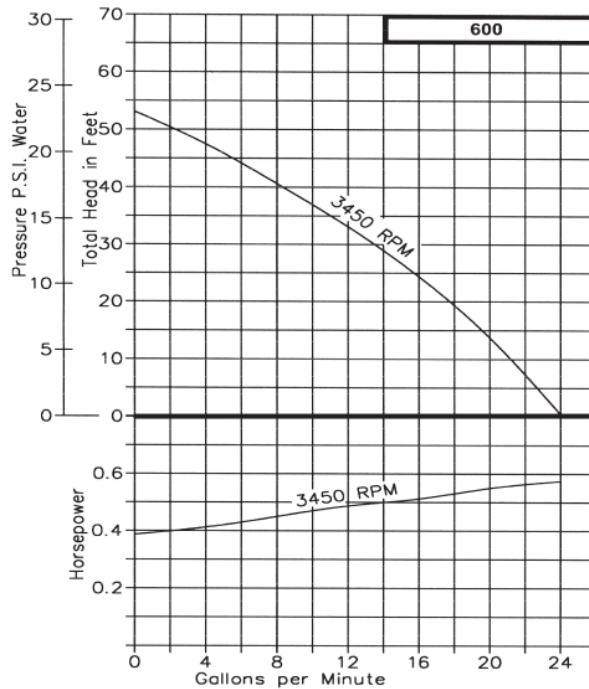


Figure 15: Water Pump Curve for Wetting Water Loop [17]

4.5 Heat Exchanger Hot Water Loop Design

The design quality of the heat exchanger hot water loop determined the entire system's performance. The heat exchanger hot water loop design is described in detail in this section.

4.5.1 Hot Water Loop Design

Figure 16 shows the diagram of the hot water loop design. The designed test heat exchanger capacity was 17 kW; therefore, using an electrical water heater to provide the heat to the water required a large amount of electricity. According to McMaster-Carr's water immersion heater's specification, a 17 kW water heater needs

more than 60A of electricity at 208V. However, this was higher than the electrical limitation of the environmental chamber where the test facility was located. Another concept for providing heat to the hot water loop was to build a heat pump. Since the typical COP of a heat pump is roughly 3, it used much less electricity to provide the design requirement of 17 kW.

There were two loops in this design. The primary loop was a hot water loop, and the secondary loop was a refrigerant loop. The inter-medium was a water-to-refrigerant plate type heat exchanger. For the primary loop, there were three main components: the ball valve, the pump and the water flow meter. The pump provided the driving force of hot water recirculation, and the ball valve was used to control the flow rate of the hot water loop. In order to record and monitor the water flow rate, a water flow meter was introduced into this design. For the secondary refrigerant loop, the main purpose was to provide the heat to the primary loop; therefore, the performance (for instance, COP) of this loop was not essential. Thus, the performance of the refrigerant loop was not recorded. However, this heat pump still needed to be designed properly for the primary loop. Besides the four components of a typical heat pump (compressor, expansion valve, evaporator, and a plate type heat exchanger as the condenser), a hot gas bypass control technology was introduced into this design. The principle of the hot gas bypass control is to add an additional bypass valve between the compressor

outlet and evaporator outlet, meaning that a certain amount of refrigerant was bypassed from the compressor discharge line back to the suction line, thus reducing the capacity of condenser without changing the speed of the compressor. By using this control strategy, the temperature of the hot water loop could be adjusted with the capacity of the condenser change.

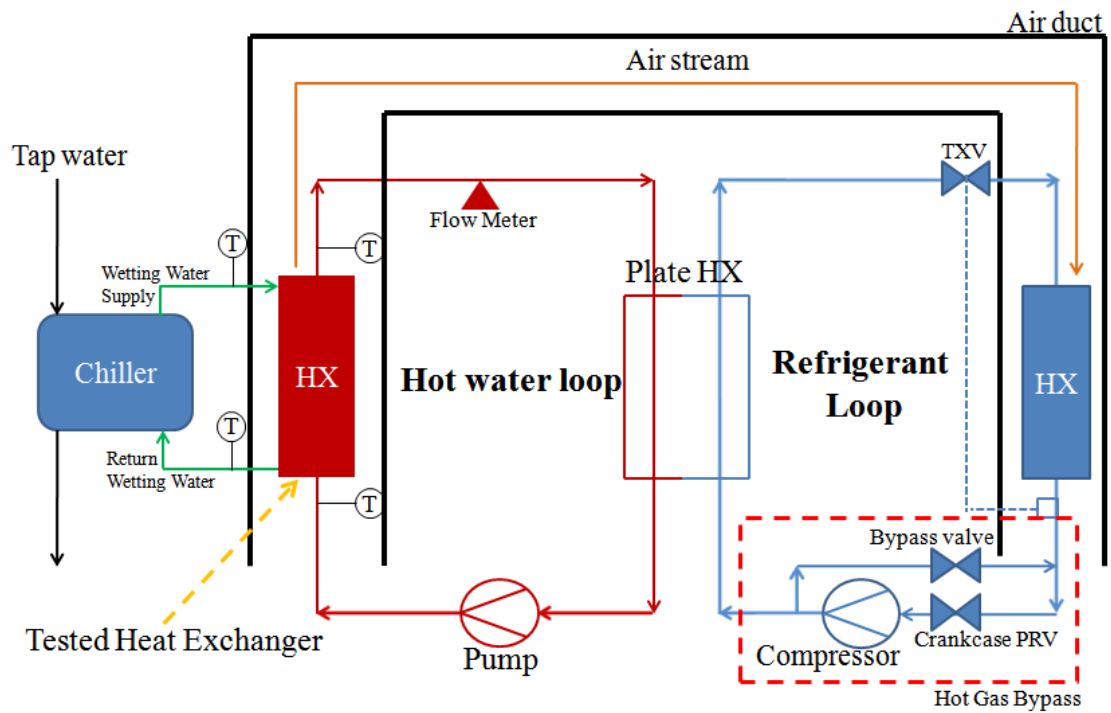


Figure 16: HX Hot Water Loop

4.5.2 Hot Water Loop Component Selection

In addition to the plate type heat exchanger and ball valve, two components needed to be sized and selected: a pump and a water flow meter in the hot water loop. For sizing the pump, two pieces of information were required. The water flow rate 1 l/s (16 GPM) was provided by the sponsor, and the total water pressure drop of the primary hot water loop was assumed to be 50 psi (3.4×10^5 Pa). There was an available pump, model HP75SS, in the CEEE Heat Pump Laboratory. The performance curve is shown in Figure 17. The bold black curve represents the performance of the pump. The pump working range covered the operating conditions of a 16 GPM (1 l/s) water flow rate at 52 psi (3.6×10^5 Pa). Therefore, this pump was selected for the project. However, by reading the performance curve, it can be seen that the system operated at the relative low flow rate range of the pump, which means that any small pressure drop increment led to a significant water flow rate decrease.

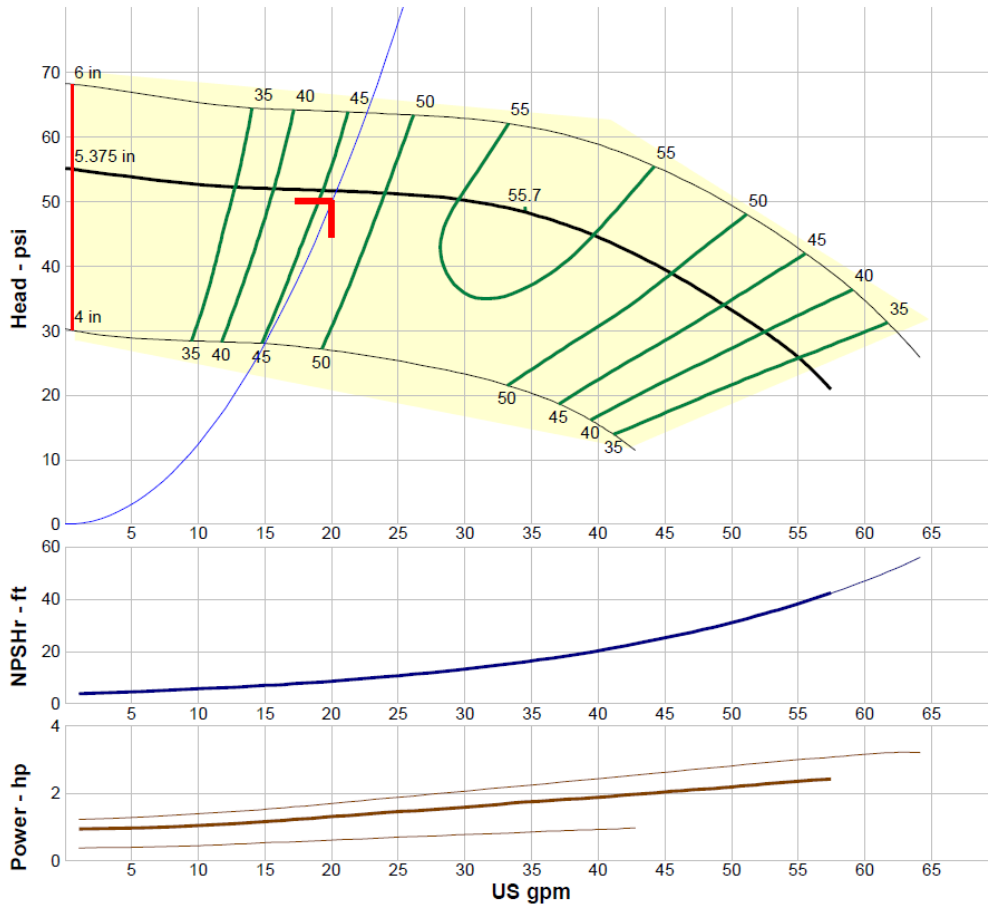


Figure 17: HP75 Pump Curve [18]

The water flow meter specifications needed to cover the design operating conditions of 16 GPM (1 l/s). Another turbine type water flow meter, Sponsler SP 1, was available and selected from the CEEE Heat Pump Laboratory. The flow meter specification is shown in Table 4.

Table 4: Hot Water Loop Flow Meter

Specifications	Values
Water Volume Flow Range	4 ~ 60 GPM (0.25 ~ 3.75 l/s)
Accuracy	±1%

Four components of the secondary refrigerant loop needed to be sized: a compressor, an expansion valve, an evaporator, and a hot gas bypass valve. The compressor was the core of the heat pump so it needed to be sized first. A Copeland scroll type, fixed speed compressor, model ZS38K4E-TF5, was selected. The working refrigerant was R-22. Because the hot water side temperature was set to between 35°C and 31°C, the condensing temperature of the heat pump was in the range around 37.8°C. Table 5 shows the performance data from Copeland’s technical report [19]. Due to the required heat of the test heat exchanger was equal to 17 kW, therefore, the heat pump could provide sufficient heat to the primary loop while the condensing temperature would be between 37.8°C and 43.3°C and the evaporating temperature would be between 35°F (1.7°C) and 45°F (7.2°C).

Table 5: Compressor Data Sheet [19]

Condensing Temperature (°C)	Parameter	Evaporating Temperature (°C)		
		1.7	4.4	7.2
43.4	Capacity (W)	15167	16625	18083
	Power (W)	4680	4910	5150
	Current (A)	13.9	14.4	15
40.6	Capacity (W)	15458	17063	18521
	Power (W)	4550	4780	5050
	Current (A)	13.6	14.1	14.7
37.8	Capacity (W)	15896	17354	18958
	Power (W)	4430	4660	4920
	Current (A)	13.3	13.8	14.4

The capacity of the heat pump was designed to be approximately 14 to 17.5 kW.

Based on the compressor selection, all other components should follow this capacity.

An available thermostatic expansion valve (TXV) in Heat Pump Lab was used as the expansion valve. Figure 18 shows the selected TXV, Sporlan SVE-8-C. The capacity of this TXV was 8 tons (28 kW), which was sufficient for the heat pump.



Figure 18: Selected Sporlan TXV

The evaporator was installed into the end of the air duct to absorb the heat from the air-flow downstream. This would enable the reuse of the waste heat from the test heat exchanger without increasing the cooling load of the environmental chamber. For selecting the evaporator, the CEEE CoilDesigner was used to estimate the capacity of the available heat exchangers in the Heat Pump Lab. There were 6 tube-fin heat exchangers, each with the same design, available in Heat Pump Laboratory. One is shown in Figure 19. The heat exchanger was a round-tube-fin heat exchanger that was made of aluminum wavy fins and copper tubes. The detailed specifications are shown in Table 6. The capacity of each heat exchanger was calculated by CoilDesigner to be 5.2 kW. Accordingly, connecting four of them in parallel provided roughly 20 kW of capacity.

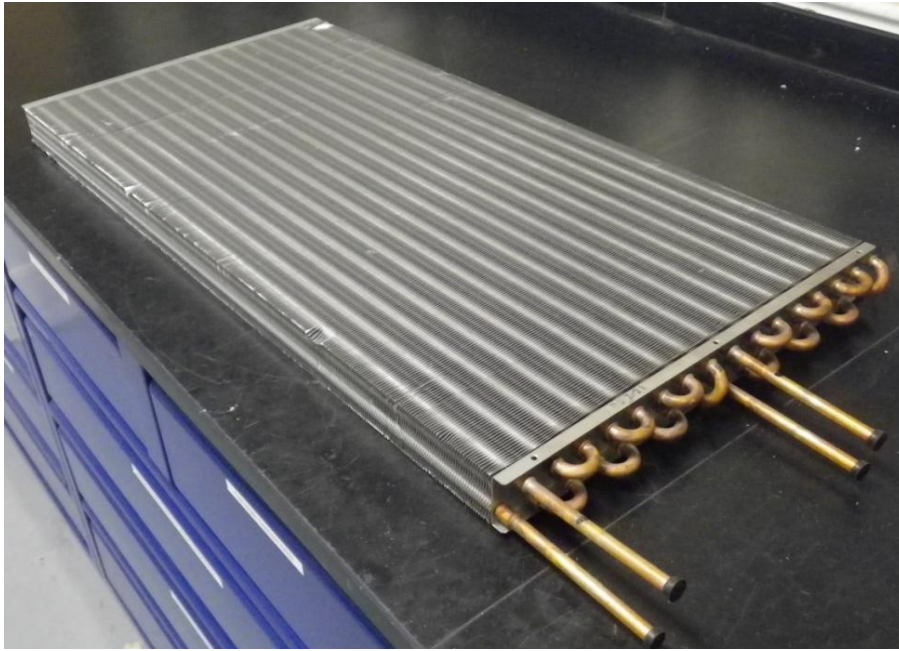


Figure 19: Tube-fin HX

Table 6: Tube-Fin HX Detailed Specifications

Parameters	Value
Width	0.38 m
Length	0.74 m
Depth	0.04 m
Fin Type	Wavy
Fin Pitch	1.6 mm
Fin Thickness	0.1 mm
Tube Pitch	25.4 mm
Tube Inner Diameter	5.4 mm
Tube Outer Diameter	6.4 mm

The last item of the hot water loop was the hot gas bypass valve. For sizing the valve, the criterion used was the Flow Coefficient, C_v [20]. It is a relative measure of its efficiency in allowing fluid flow. It describes the relationship between the pressure drop across an orifice, valve or other assembly, and the corresponding flow rate. The mathematical definition is as follows:

$$C_v = F\sqrt{SG/\Delta P} \quad \text{Equation 10}$$

Where F is fluid volume rate (GPM), SG is specific gravity of fluid (Water = 1), and ΔP is the pressure drop across valve (psi).

Based on the known refrigerant properties, the highest required C_v of the hot gas bypass valve could be calculated to be 1.3. A metering valve, Swagelok SS-12NRS12, was available, and is shown in Figure 20. According to the manufacturer's specification, the C_v of this valve was 2.4. Therefore, this valve could be used in the hot gas by pass loop.

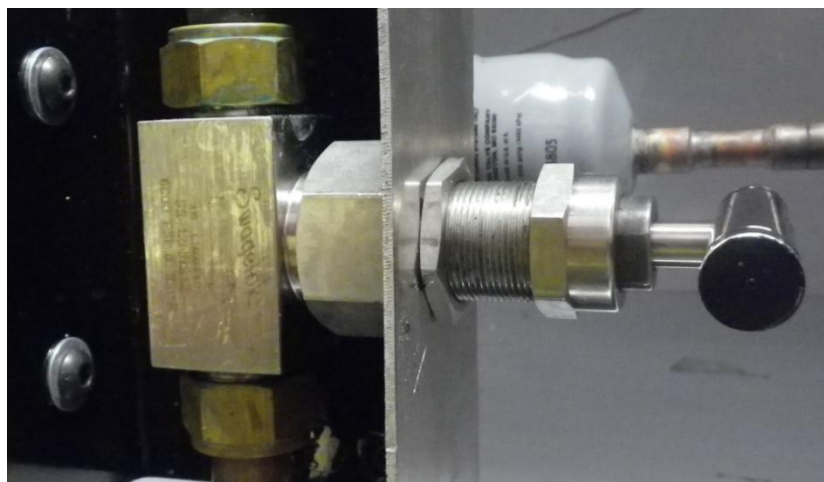


Figure 20: Hot Gas Bypass Valve

5. Test Facility Construction

The overview of the test facility is shown in Figure 21. This figure includes the air side, the wetting water side, the primary HX hot water side, and the secondary refrigerant side. The construction for each side is described in detail in the following sections.

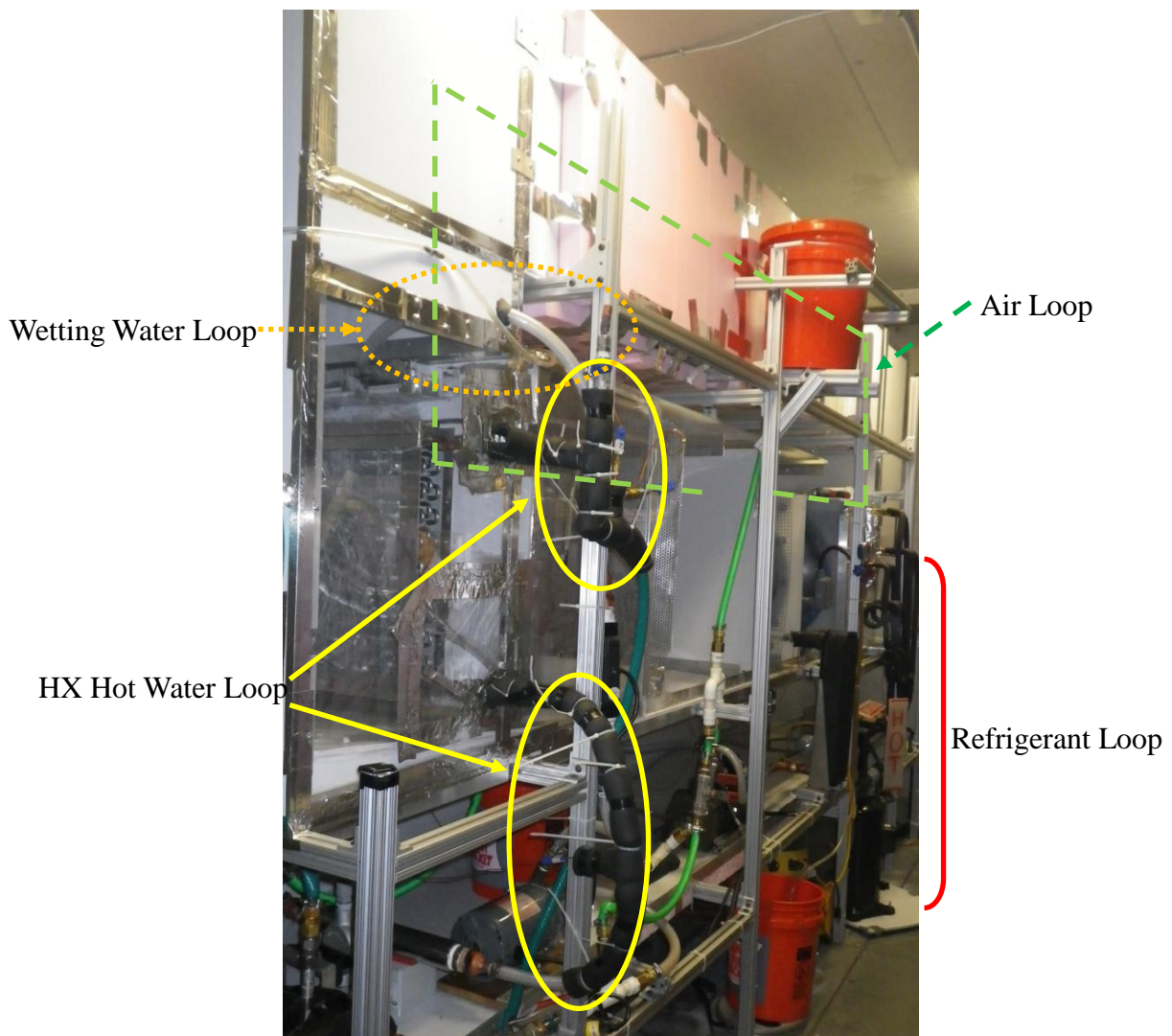


Figure 21: The Overview of the Test Facility

5.1 Air Duct Construction

There was an existing air duct in the CEEE Heat Pump Laboratory, which was well constructed for a previous finished project. Fortunately, the dimension of the existing air duct satisfied the air duct design requirement, in addition to saving construction time. Figure 22 shows the existing air duct before being taken over by this project.



Figure 22: The Existing Air Duct in CEEE Lab.

Because the air duct configuration was not identical to the original design, the proper rearrangement and modifications were needed for both the existing air duct and the original design. Figure 23 shows the rearrangement and connection between the existing wind tunnel and the current design. Both the nozzles and the temperature measurement were moved up to the top of the facility. Instead of blowing air into the wind tunnel, the air fan was moved down to the end of the air duct, where it sucked the air from the system. Third, the test section was relocated to the front corner of the

system, and placed in front of the air nozzles. With this configuration, the temperature measurement in front of the air nozzles became the outlet condition, and the inlet condition measurements preceded the test section.

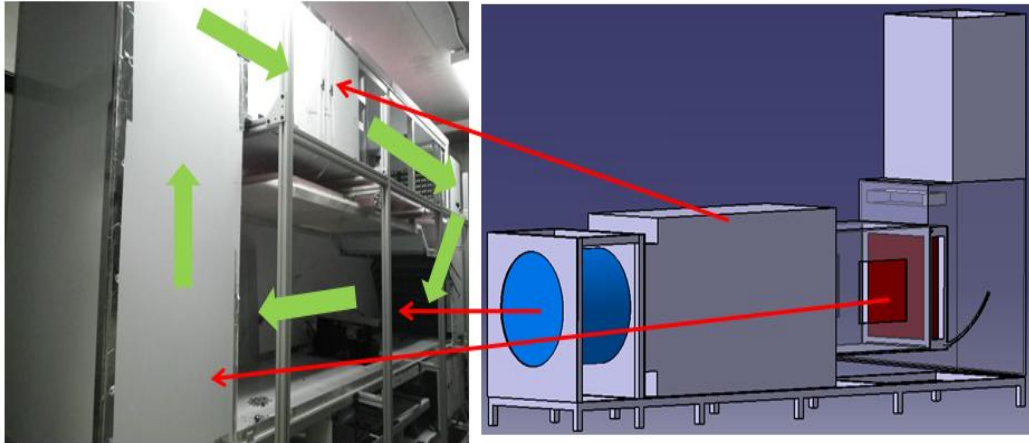


Figure 23: Rearrangement of the Air Duct

Figure 24 shows the modified test facility. Although the arrangement was changed, the facility still followed the ASHRAE Standard 41.2 [15] as mentioned in the previous section (Figure 7 and Figure 8), and the design principle remained the same.

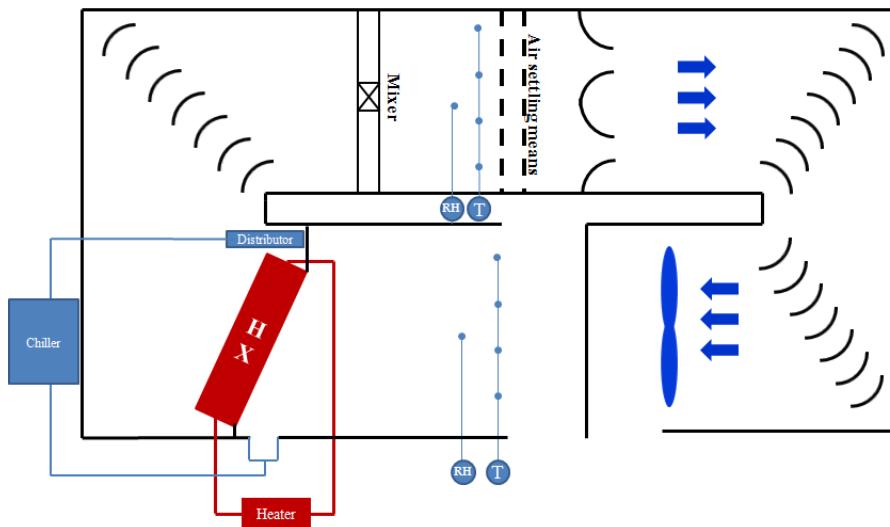


Figure 24: Modified Test Facility

Figure 25 shows the modified dimension of the test facility.

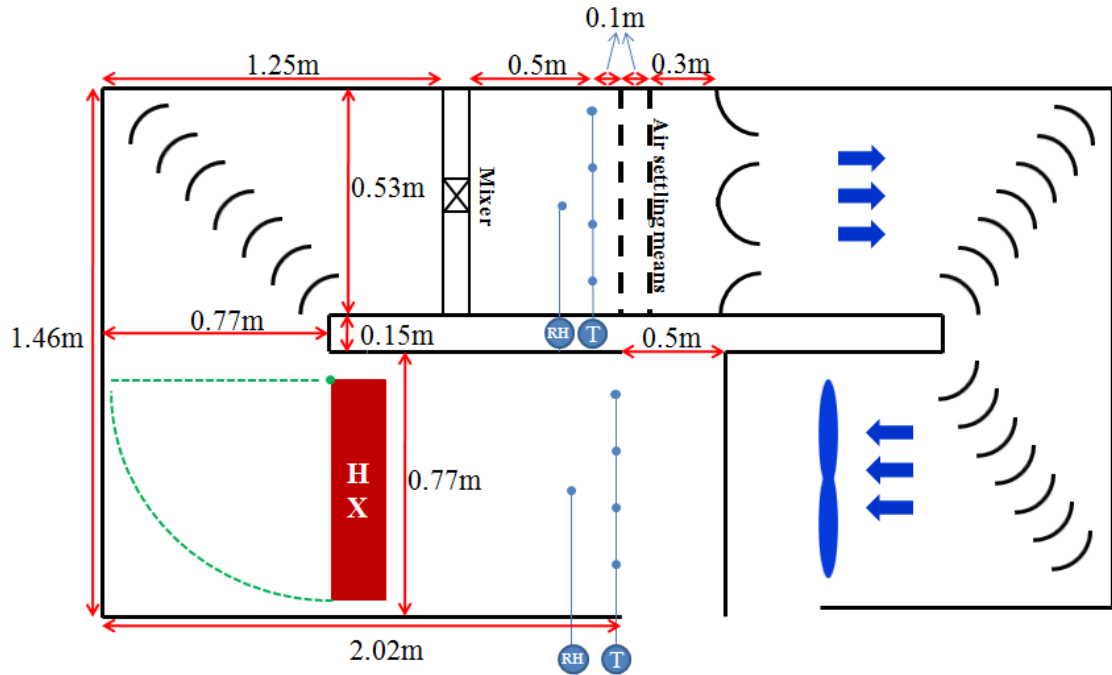


Figure 25: Modified Dimension of the Test Facility

Figure 26 through Figure 30 show the construction of the wind tunnel components and air fan installation.

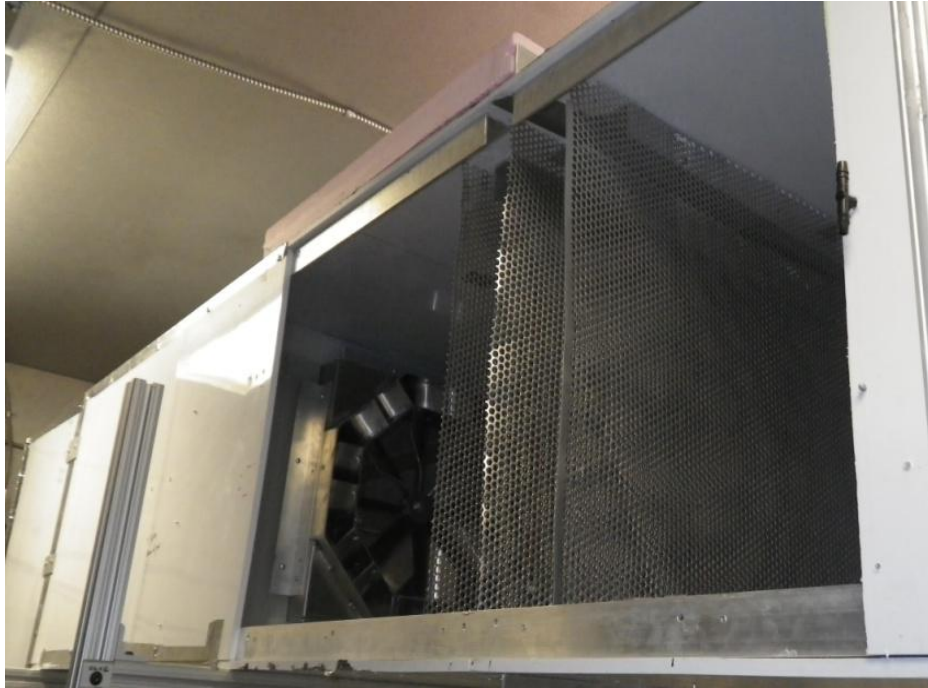


Figure 26: Air Mixer and Flow Settling Means

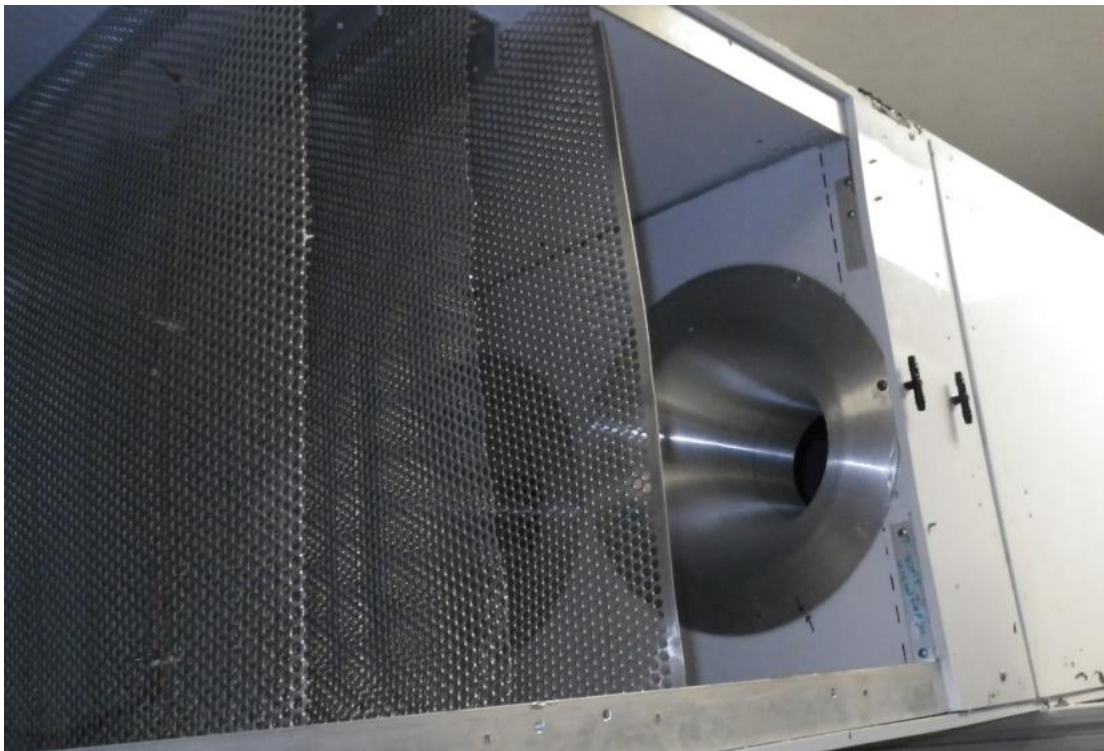


Figure 27: Air Flow Settling Means and Air Nozzles

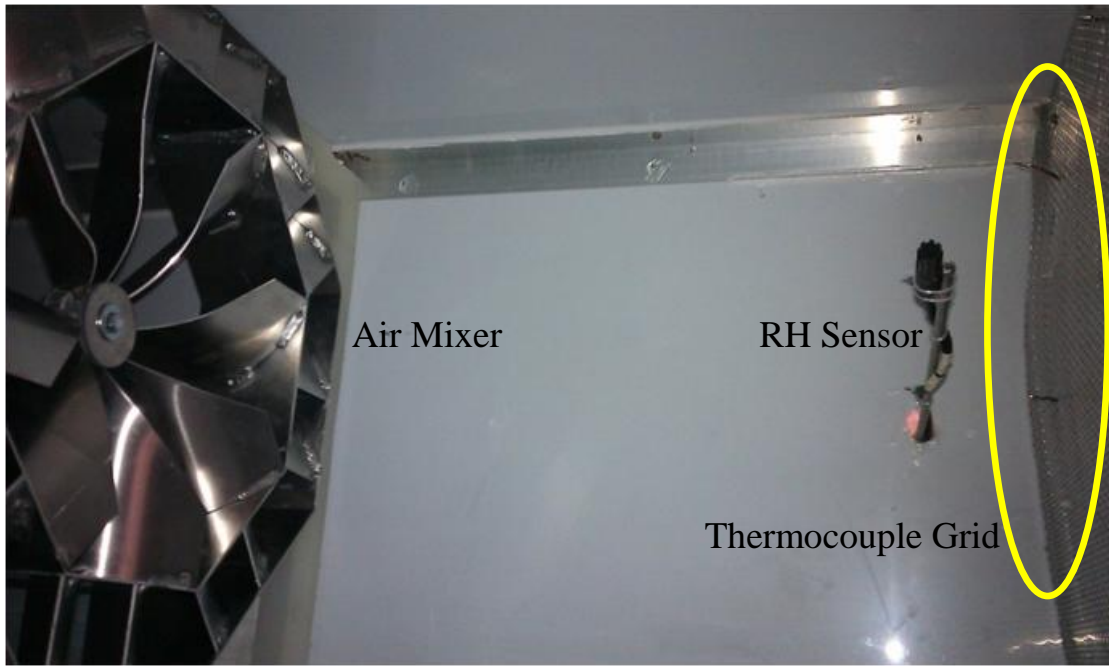


Figure 28: Air Mixer, RH sensor and TC Grid



Figure 29: RH Sensor, TC Grid and Air Flow Settling Means

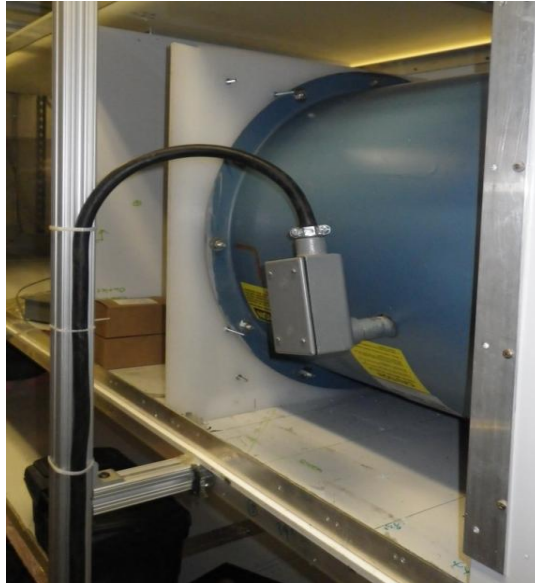


Figure 30: Axial Fan Installation

5.2 Wetting Water Loop Construction

Figure 31 shows the chiller, which is located outside of the chamber. The PVC pipes transport the supply return water.



Figure 31: The Chiller

Figure 32 shows the plate heat exchanger, model: Alfa Laval AC120-40HQ-S46, installation of the wetting water loop. The plate type heat exchanger was positioned horizontally because it was a water-to-water heat exchanger. Meanwhile, the wetting water flow meter also can be seen in this figure.



Figure 32: Wetting Water Side Plate HX

The wetting water distributor is shown in Figure 33. This distributor was designed to allow 0.16 l/s wetting water. The holes on the bottom of the distributor allowed the wetting water to evenly distribute the wetting water on the heat exchanger.



Figure 33: Wetting Water Distributor

5.3 Heat Exchanger Hot Water Loop Construction

The hot water loop plate type heat exchanger, model: FlatPlate CH5, is shown in Figure 34. The difference between this one and the one in the wetting water loop was the orientation of the heat exchanger. This plate heat exchanger was installed vertically because the effect of condensing on the refrigerant side must be taken into consideration. Accordingly, the refrigerant flowed from the top to the bottom, and then in the reverse direction for the hot water side.



Figure 34: The Hot Water Loop Plate HX

Figure 35 shows the secondary refrigerant loop for the hot water loop. The evaporator was installed in the air duct to absorb the heat from the air stream.



Figure 35: Secondary Refrigerant Loop

Figure 36 shows an additional construction from the original design. This water charge system was used to charge the water to both hot water loop and wetting water loop. There were two valves to control the water charge amount for each water side. Since this charge system was only working by gravity force, the water reservoir (the orange bucket in the figure) was installed at the highest point of the entire system.

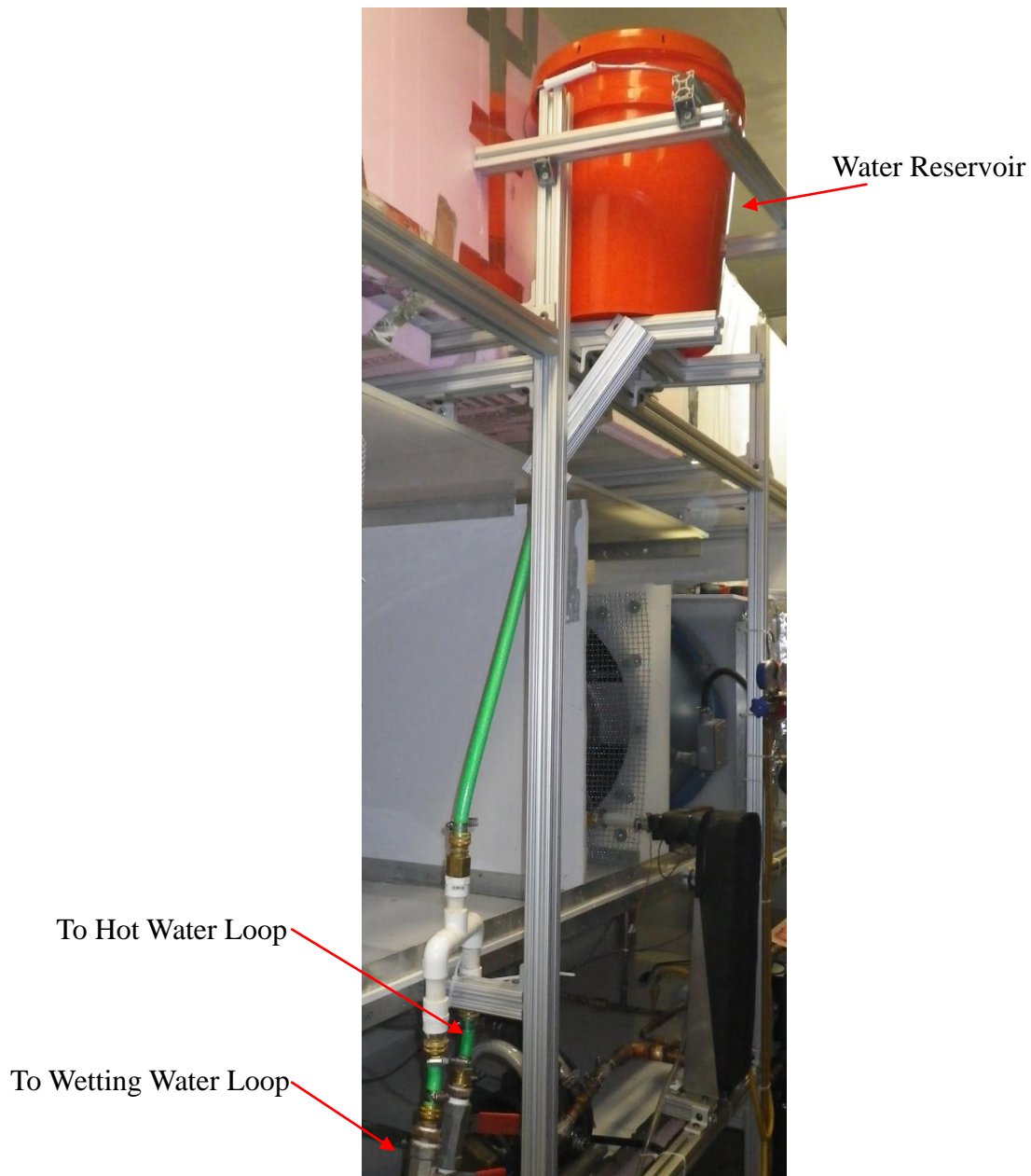


Figure 36: Water Loops Charge System

6. Experimental Work

6.1 Instrument Calibration

6.1.1 Humidity Sensor Calibration

In order to measure the air side of heat exchanger inlet and outlet, two humidity sensors needed to be installed; however, due to the age of the humidity sensors, calibration was required for both sensors. The humidity sensors were calibrated using the Vaisala Humidity Calibrator HMK15. The function of calibration is based on the fact that certain salt solutions generate specific relative humidity conditions at certain ambient atmospheric temperatures above them. This calibration was conducted by using three different salts: MgCl_2 , NaCl , and K_2SO_4 . The entire set of humidity sensor calibrators was placed in an environmental chamber in order to maintain the ambient temperature at a certain degree. The calibration was based on Greenspan's Calibration Table [21], which is shown in Table 7.

Table 7: Greenspan's Calibration Table [21]

°C	MgCl ₂ (%)	NaCl (%)	K ₂ SO ₄ (%)
0	33.7±0.3	75.5±0.3	98.8±1.1
5	33.6±0.3	75.7±0.3	95.5±0.9
10	33.5±0.2	75.7±0.2	98.2±0.8
15	33.3±0.2	75.6±0.2	97.9±0.6
20	33.1±0.2	75.5±0.1	97.6±0.5
25	32.8±0.2	75.3±0.1	97.3±0.5
30	32.4±0.1	75.1±0.1	97.0±0.4
35	32.1±0.1	74.9±0.1	96.7±0.4
40	31.6±0.1	74.7±0.1	96.4±0.4
45	31.1±0.1	74.5±0.2	96.1±0.4
50	30.5±0.1	74.4±0.2	95.8±0.5

For each calibration point, the relative humidity required 24 hours to reach steady state. The calibration setup is shown in Figure 37. Each salt solution was in a separate container, and both humidity sensors could be calibrated at the same time.



Figure 37: Humidity Sensor Calibrator

Figure 38 and Figure 39 show the calibration results of the humidity sensors. The calibration was done under the ambient temperature of 31°C. According to Table 7, the calibration errors at this temperature for each salt solution, MgCl₂, NaCl, and K₂SO₄, are ±0.1%, ±0.1%, and ±0.4%, respectively. Further, the calibration range was from 30% to nearly 100%, for both humidity sensors, and the calibration results show that the coefficient of determination R² of the trend lines are both larger than 0.9999, so the results show the great linearity of the humidity and the output signal.

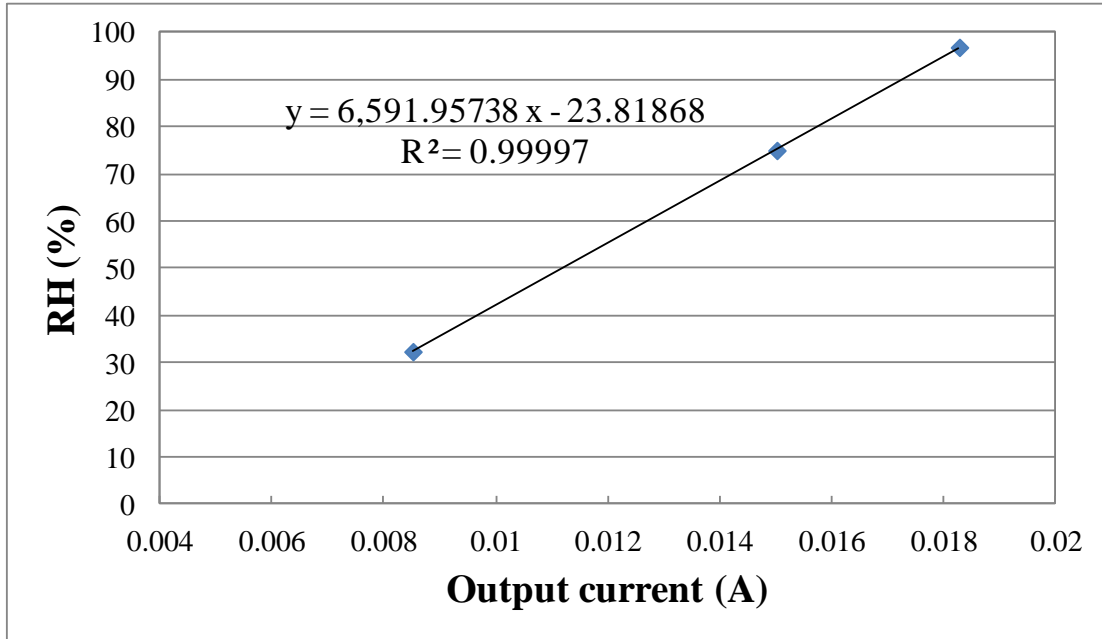


Figure 38: Calibration Result of RH Sensor #1

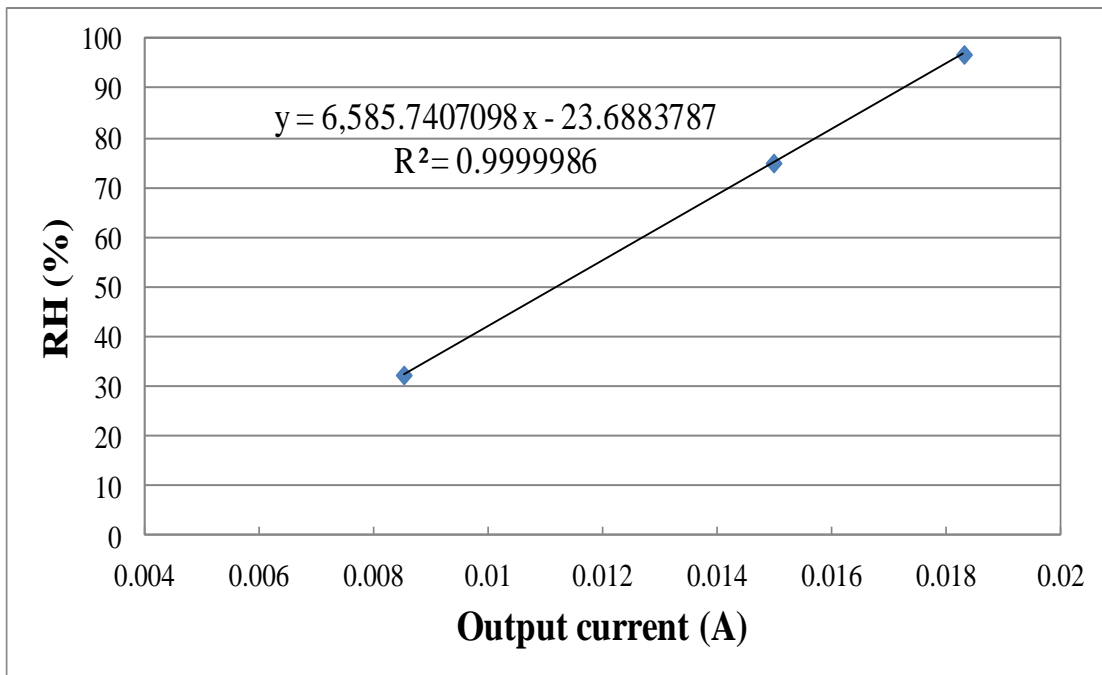


Figure 39: Calibration Result of RH Sensor #2

6.1.2 Air Nozzle Calibration

The purpose of the nozzles was to measure the air-flow rate of the wind tunnel, and the air frontal velocity of the tested heat exchanger can be determined by the air-flow rate. Even though the wind tunnel and the nozzles were constructed and manufactured based on ASHRAE Standard [15], the calibration still needed to be done in order to obtain an accurate air flow measurement. Based on ASHRAE Standard 41.2, Standard Methods for Laboratory Airflow Measurement [15], the air volume flow rate can be calculated by measuring the air properties and nozzle air side pressure drop. There were two air nozzles in the wind tunnel, both of which were manufactured based on ASHRAE Standard 41.2 [15]. Figure 40 shows the standard geometry of the air nozzles.

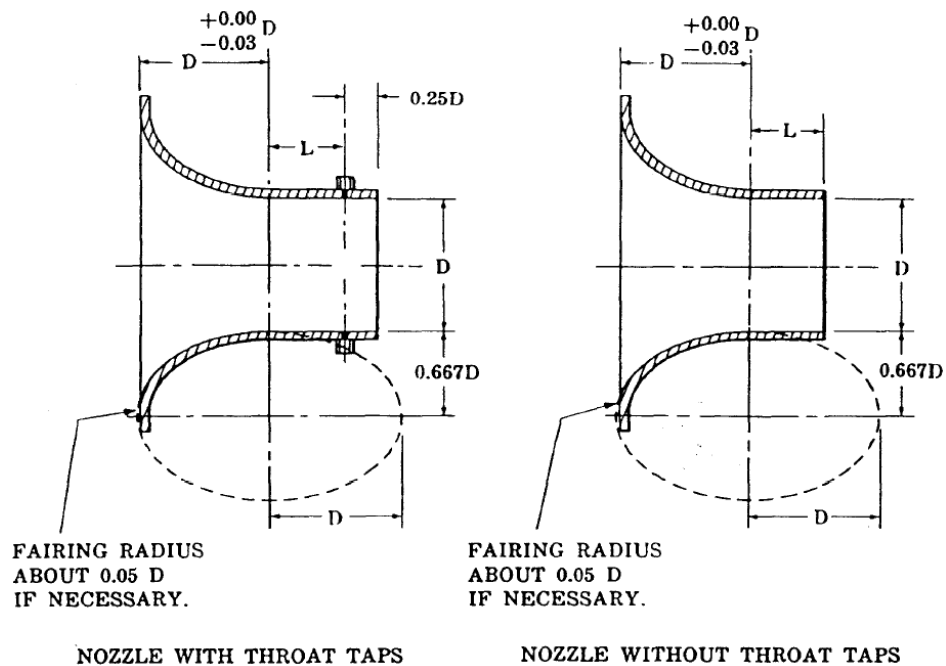


Figure 40: ASHRAE Standard Nozzle [15]

The nozzles and the differential pressure measurement of the nozzles were properly installed in the wind tunnel (see Figure 27), and the ideal air volume flow rate can be calculated based on the following equations:

$$Q_{id} = (\sum CA_n)Y(2\Delta P_n/\rho_o) \quad \text{Equation 11 [15]}$$

Where

$$Y = 1 - (0.548 + 0.71\beta^4)(1 - \alpha) \quad \text{Equation 12 [15]}$$

Where

$$\alpha = 1 - \left[\Delta P_n / [\rho_o R(T_o + 273.2)] \right] \quad \text{Equation 13 [15]}$$

$$\beta = D_n/D_d \quad \text{Equation 14 [15]}$$

C is the nozzle discharge coefficient, which is the coefficient of the nozzle Reynolds Number (Re). According to ASHRAE Standard 41.2 [15], an approximation of acceptable accuracy for temperature from 4.4°C to 37.8°C is:

$$Re = 70900D_n [(\Delta P_n \rho_o) / (1 - \beta^4)]^{0.5} \quad \text{Equation 15 [15]}$$

The principle of this calibration was energy balance. Figure 41 shows the layout of the heat source chamber for calibrating the air nozzles. This chamber was connected to the air nozzles section. From the energy balance, the heat input and the heat dissipation should be identical. The inlet and outlet temperatures, and the relative humidity of the heat source, can be measured with the thermocouples grids and humidity sensors. Once the theoretical air volume flow rate is calculated based on

Equation 11, the heat dissipation of air can be calculated using the following equation:

$$E_a = Q_{id}\rho_o C_p(T_o - T_i) \quad \text{Equation 16}$$

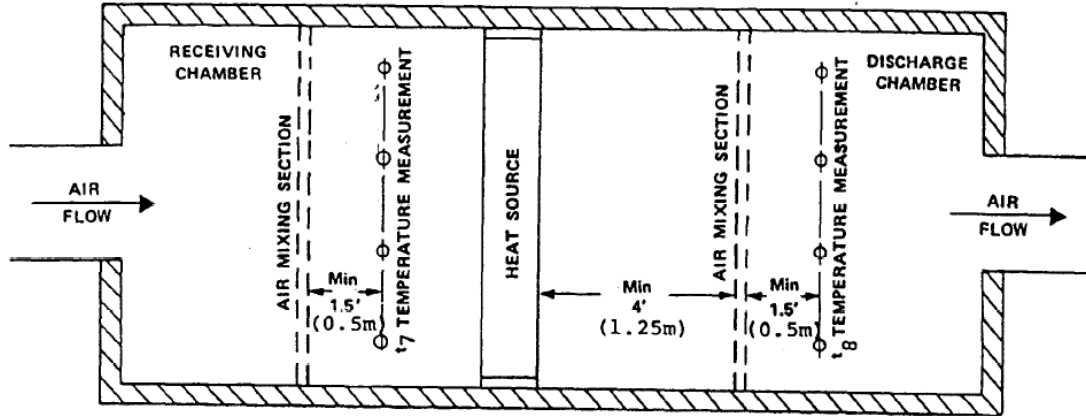


Figure 41: Air Nozzle Calibration Chamber [15]

Electrical air heaters (Figure 42) were used as the heat source in this calibration, and the energy input from the heaters was measured using the wattage meter shown in Figure 43. In order to minimize the air side temperature measurement uncertainty, ASHRAE Standard 41.2 suggests that the temperature difference across the heat source should be greater than 10°C. Therefore, in order to follow the Standard, the air heater capacity was sized using the following calculation:

Designed highest heat exchanger frontal air velocity: 3.5 m/s

Purposed heat exchanger frontal area: 0.25 m²

Purposed ambient air condition: 22°C, 50% relative humidity

$$E_h = \dot{m}_{air} \times C_p \times \Delta T$$

$$E_h = 10.83 \text{ kW}$$

Therefore, the capacity of the air heaters should be at least 10.83 kW. In this calibration, a 12 kW air heater set was installed so as to precede the air nozzles in the wind tunnel. The distances between each component followed the ASHRAE Standard as shown in Figure 41.



Figure 42: Electrical Air Heaters



Figure 43: Wattage Meters

The actual air volume flow rate can be calculated using the following equation based on the measured air heater power:

$$Q_{\text{act}} = E_h / [\rho_o C_p (T_o - T_i)] \quad \text{Equation 17}$$

The theoretical air side dissipation capacity could be determined using Equation 11, and the actual energy input could be measured using the wattage meter of the air heaters. By comparing the theoretical and actual capacity, the nozzle discharge coefficient could be adjusted based on the actual capacity, which was measured using the wattage meter.

Table 8 shows the results of the actual air-flow rate (measured from the air heater capacity) and the ideal air-flow rate (calculated from the ASHRAE equations) of a single nozzle. By varying the frequency of the fan inverter to provide different air-flow rates, the flow rate effectively covered the complete working range of a single nozzle (see Equation 5 and Equation 6). The deviations between the actual air-flow rate and the ideal flow rate were less than 3%, which showed that the air nozzles could accurately measure the air flow rate within the low flow rate region.

Table 8: Nozzle Calibration: AFR of Single Nozzle

Air Fan Inverter Frequency (Hz)	Q _{actual} (m ³ /s)	Q _{Ideal} (m ³ /s)	Deviation (%)
34	0.43	0.42	2.55
30	0.37	0.37	2.10
25	0.31	0.31	1.63
20	0.25	0.24	2.50
18	0.23	0.22	2.41

The actual and ideal air-flow rates of a single nozzle vs. the air fan inverter frequency are shown in Figure 44. The graph shows that the relationships between the flow rates and Re were both highly linear because the coefficients of determination (R^2) of both actual and ideal flow rates were very close to 1.

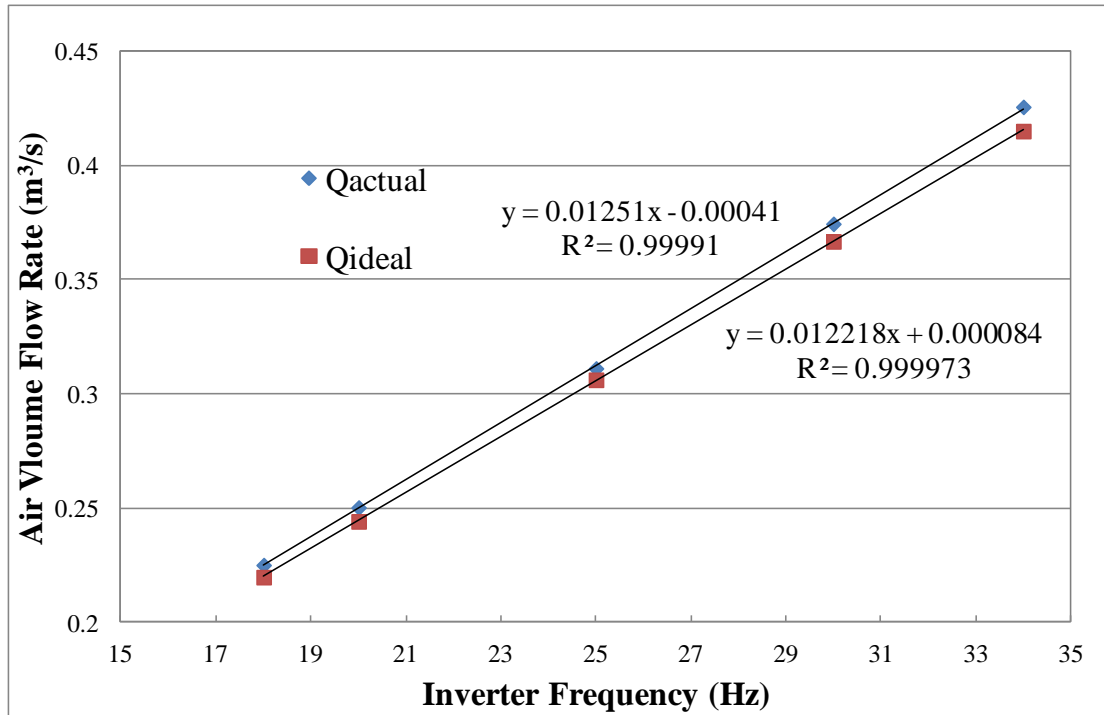


Figure 44: Nozzle Calibration: AFR of Single Nozzle

Table 9 shows the Reynolds number and the discharge coefficients C of different air-flow rates of the single nozzle. This table shows both the ideal C (from ASHRAE Standard [15]) and the adjusted C (by measuring and calculating). Certainly, the adjusted C will be used in the following experiments. Meanwhile, the deviations between the ideal C and the adjusted C were shown in this table, as well. Because the C was also calculated from Equation 11, the deviations were identical to those seen in Table 8. Furthermore, because all adjusted C were nearly the same, the average value 1.004 was used in the following experiments.

Table 9: Nozzle Calibration: Discharge Coefficient of Single Nozzle

Reynolds Number, Re	C	Adjusted C	Deviation (%)
231454	0.985	1.010	2.55
202342	0.984	1.004	2.10
166011	0.982	0.998	1.63
129107	0.980	1.004	2.50
114242	0.979	1.003	2.41

Figure 45 shows the discharge coefficients vs. the Reynolds number of single nozzle.

It clearly shows that all ideal C values were nearly constant and the adjusted C values fluctuated slightly around the average value 1.004.

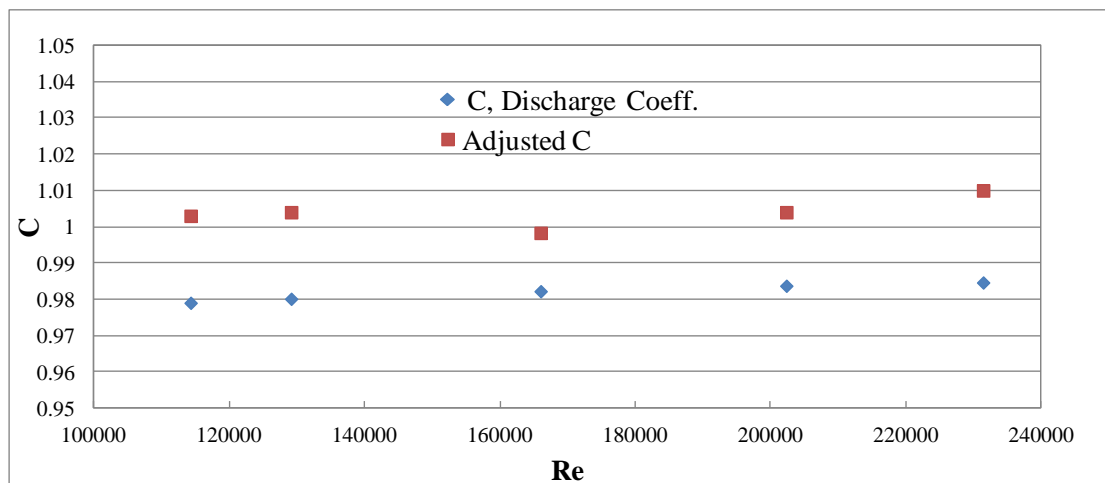


Figure 45: Nozzle Calibration: Discharge Coefficient of Single Nozzle

Because there were two nozzles in the nozzle grid, both nozzles needed to be calibrated. Table 10 shows both actual and ideal air-flow rates of two nozzles at different air fan inverter frequencies. The calibrated range covered the working range of two nozzles as well (see Equation 7 and Equation 8). This table also shows the deviation between the actual and ideal flow rates. However, the margins of errors were increased in this high flow rate region. The deviation increased from 3.6% at $0.42 \text{ m}^3/\text{s}$ to 9% at $0.75 \text{ m}^3/\text{s}$.

Table 10: Nozzle Calibration: AFR of Two Nozzles

Air Fan Inverter Frequency (Hz)	$Q_{\text{actual}} \text{ (m}^3/\text{s)}$	$Q_{\text{Ideal}} \text{ (m}^3/\text{s)}$	Deviation (%)
36	0.82	0.75	9.03
30	0.67	0.63	7.22
25	0.55	0.52	5.35
20	0.43	0.42	3.64

Figure 46 shows both the actual flow rate and the ideal flow rate vs. the air fan inverter frequency. The determination coefficients of both flow rates were larger than 0.999, which shows the high linearity for both flow rates against inverter frequency. Meanwhile, this graph also shows that the deviation between actual and ideal flow rates increased as the inverter frequency increased. This scenario shows that the air

nozzles calibration was essential for this project, especially in a relatively high flow rate region.

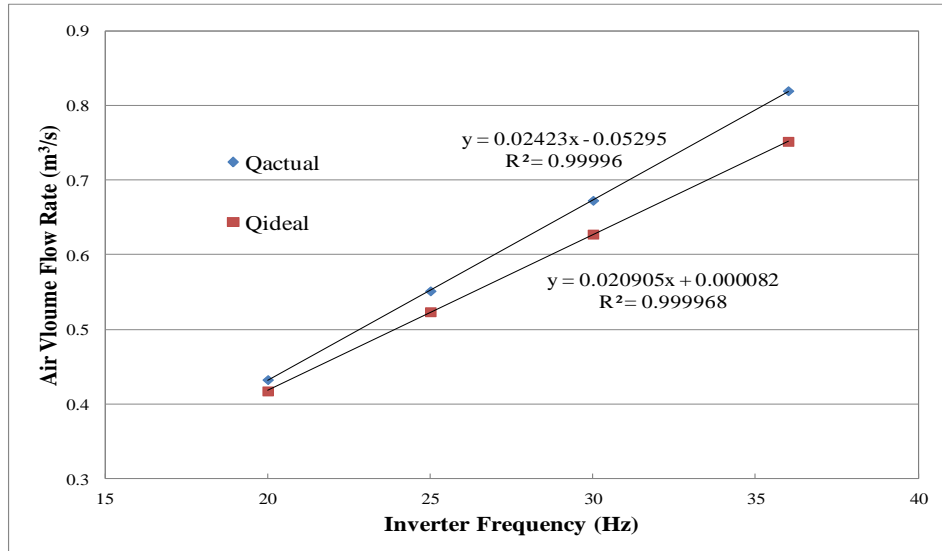


Figure 46: Nozzle Calibration: AFR of Two Nozzles

Table 11 shows the discharge coefficient, C , and the adjusted C for calibrating two nozzles, and for different Reynolds Number, Re . The deviations between C and adjusted C were also identical to the deviations of flow rates.

Table 11: Nozzle Calibration: Discharge Coefficient of Two Nozzles

Reynolds Number, Re	C	Adjusted C	Deviation (%)
216675	0.9842	1.073	9.03
179359	0.9828	1.054	7.22
148327	0.9813	1.034	5.35
116602	0.9792	1.015	3.64

Figure 47 shows the theoretical and adjusted discharge coefficient vs. the Reynolds number. This graph clearly shows that the theoretical C remained nearly constant. However, the adjusted C had a trend of linear increase. This trend also shows that the errors between theoretical and adjusted C were increasing linearly in the high Re region that is indicative of high flow rates. The linear correlation of the adjusted C, $C = 6 \times 10^{-7} \times Re + 0.9474$, was used in the following experiments to predict the flow rate of the wind tunnel.

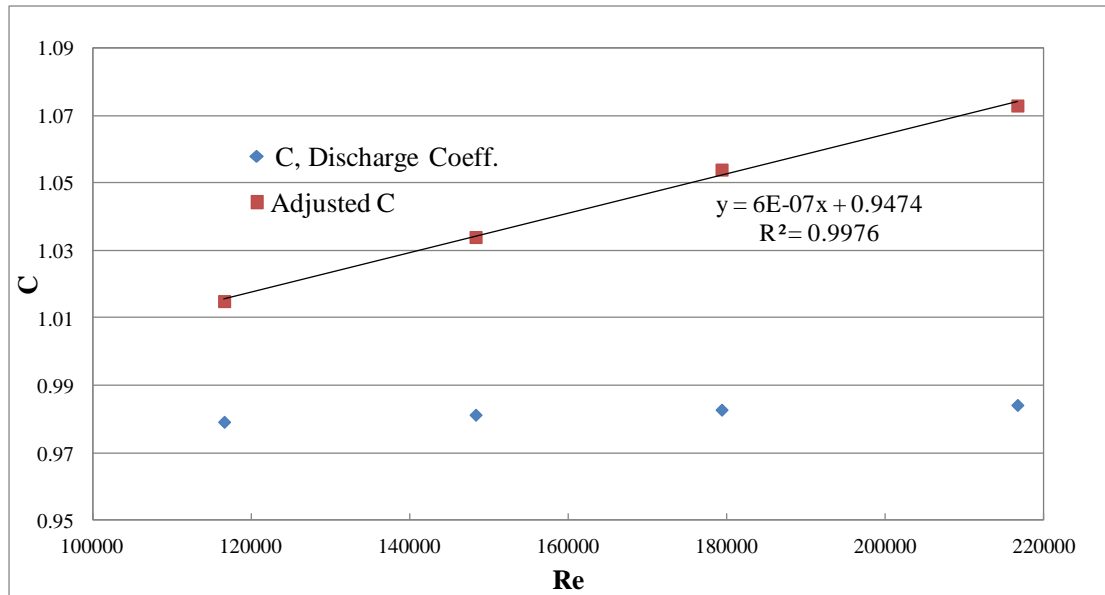


Figure 47: Nozzle Calibration: Discharge Coefficient of Two Nozzles

6.1.3 Water Flow Meter Calibration.

There were two water loops in this system. For each side, an accurate water flow meter was necessary to measure the water flow rate precisely. Accordingly, the water flow meters needed to be well calibrated.

Figure 48 shows the basic set-up of water flow meter calibration. The tap water flowed from the right via the flow meter and a metering valve, then to the bucket that was used to collect the water. An accurate scale and stopwatch were used to measure the amount of the collected water and the calibrating time. The water flow was controlled using the metering valve to ensure that the calibration range covered the proposed working flow rate. The calibration results for both water flow meters are shown in the next sections.



Figure 48: Water Flow Meter Calibration Set-up

6.1.3.1 Hot Water Flow Meter Calibration

Figure 49 shows the calibration result of the hot water flow meter. The result shows that the sensor signal voltage output had a highly linear relationship ($R^2=0.998$) with the flow rate in the calibrated range from 5 GPM (0.3 l/s) to 7.5 GPM (0.47 l/s). This

relationship, $GPM = 3.420 \times V + 25.602$, was used in the experiments to obtain the water volume flow rate and for all other calculations.

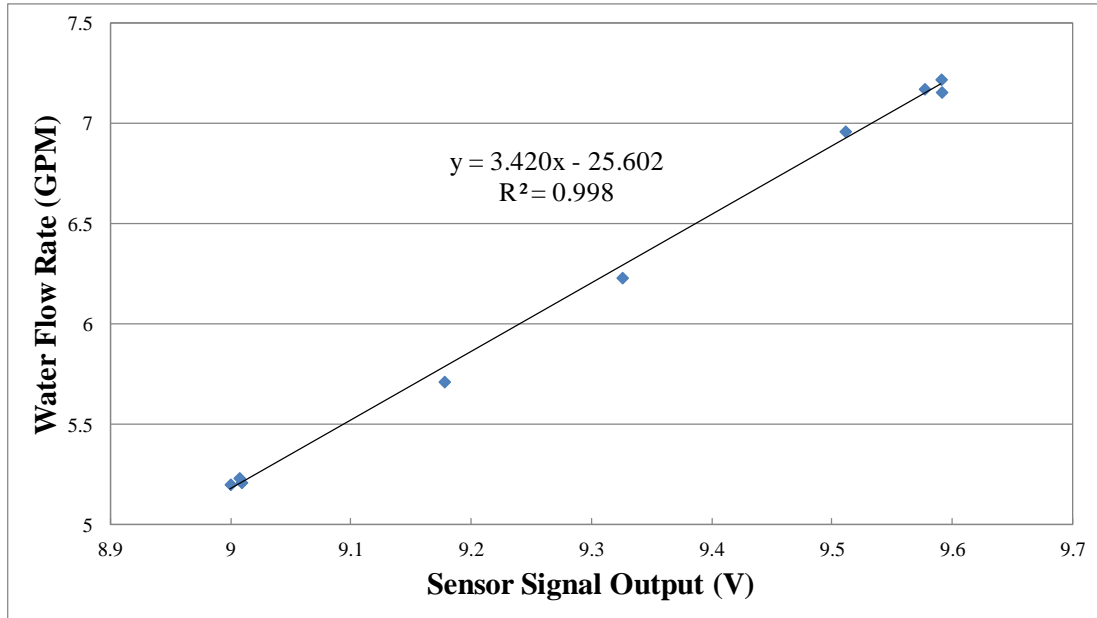


Figure 49: Hot Water Flow Meter Calibration

6.1.3.2 Wetting Water Flow Meter Calibration

Figure 50 shows the calibration result of the wetting water flow meter. Because the flow rate requirement was smaller than it was for hot water, the capacity of the flow meter was smaller and it was easier to calibrate, with higher accuracy. The results show that the sensor signal voltage output had a highly linear relationship ($R^2=0.999$) with the flow rate in the calibrated range from 2.5 GPM (0.16 l/s) to 4.3 GPM (0.27 l/s). The correlation of the sensor signal voltage output (V) and the flow rate (GPM), $GPM = 3.173 \times V + 20.772$, was used to predict the wetting water flow rate for the future experiments.

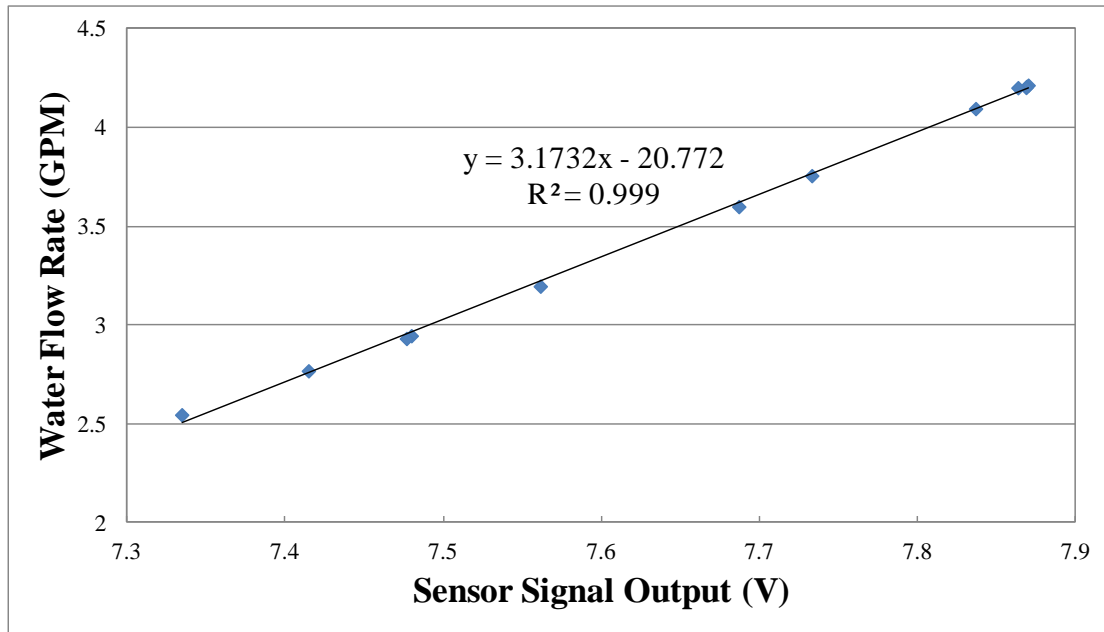


Figure 50: Wetting Water Flow Meter Calibration

6.1.4 Temperature Sensor Calibration

In order to measure the air side temperature more accurately, all the thermocouples were calibrated. In total, there were 18 thermocouples in two grids. Although combining nine T-type thermocouples in parallel for each grid usually provides accurate temperature measurement, the calibrations were still necessary to eliminate any possible uncertainty in this project. Figure 51 shows the thermocouples calibration set-up. The temperature of the water/glycol reservoir of this machine was controlled precisely to maintain a certain constant temperature. A very accurate RTD sensor, with an accuracy of 0.01°C, was also used in the calibrations. The calibration method was to dip the thermocouples, along with the RTD, into the water/glycol

reservoir. After the temperature of the reservoir and the RTD reached a steady state, the temperatures of the thermocouples were recorded.

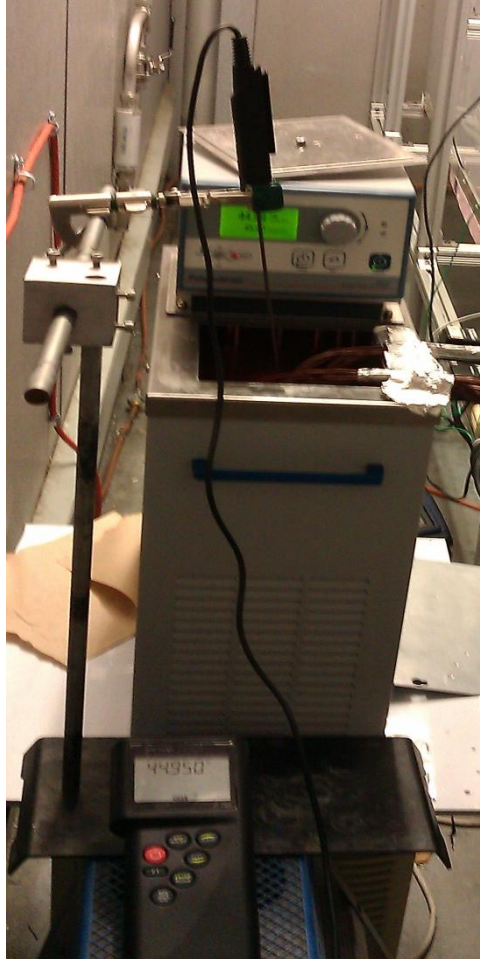


Figure 51: Thermocouples Calibration Set-up

Figure 52 shows the results of the air side inlet thermocouples calibrations. Although the accuracy of the T-type thermocouple is 0.5°C , these graphs clearly show that the thermocouples performed very well. The slope of all trend lines was very close to 1, and the y-intercepts were much smaller than 0.5, as well. Meanwhile, all the calibration results had very high linearity. The same scenario also can be seen in Figure 53. All air side outlet thermocouples performed very well.

Even though the calibration results did not show a significant difference between an un-calibrated and a calibrated thermocouple, the temperature measurement calibrations were still essential for the purpose of minimizing the experiment uncertainties. Accordingly, the correlation from all calibrations will be applied to the following experiments.

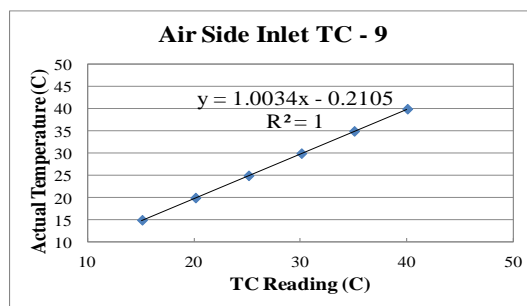
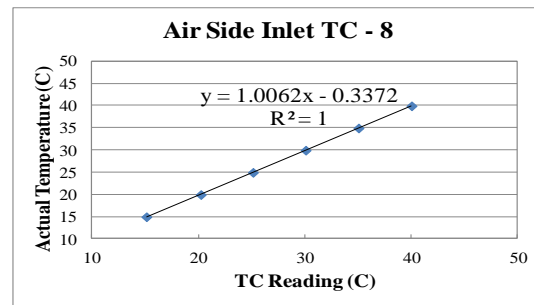
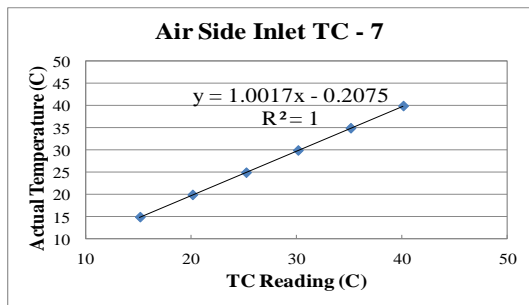
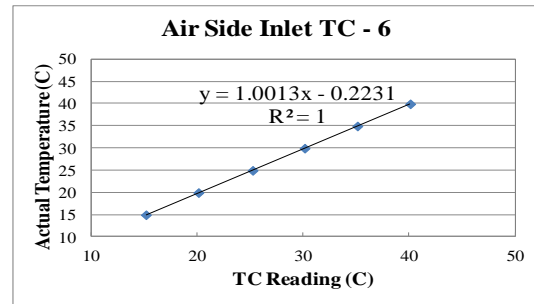
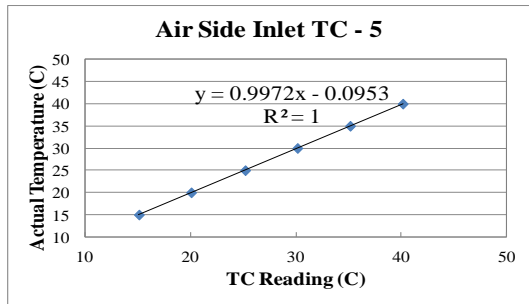
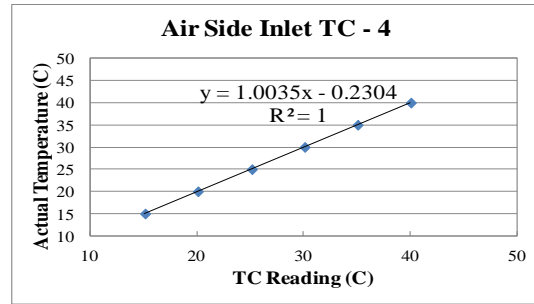
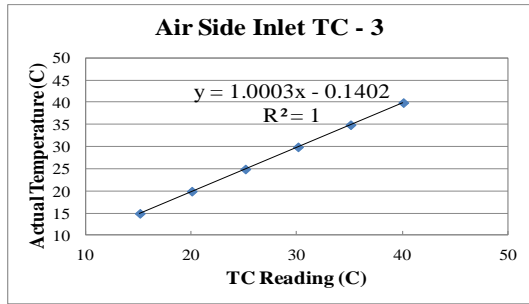
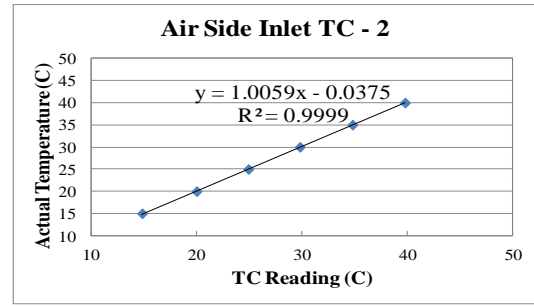
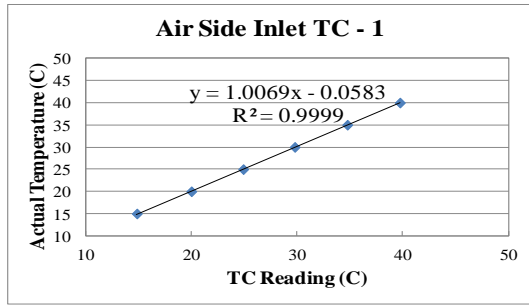


Figure 52: Air Side Inlet Thermocouples Calibration

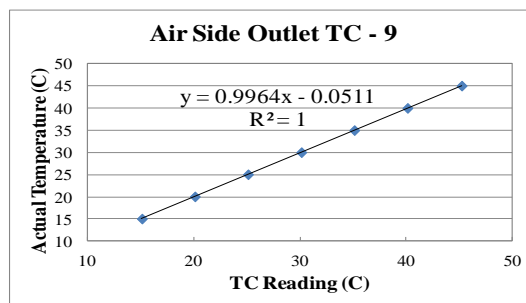
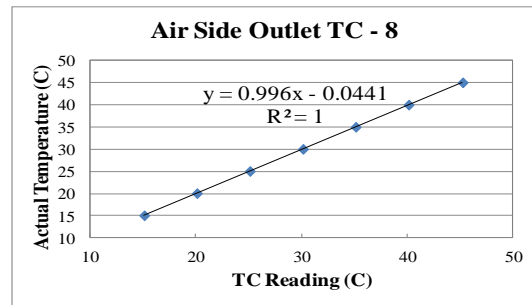
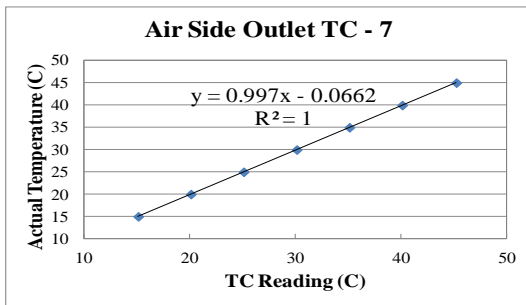
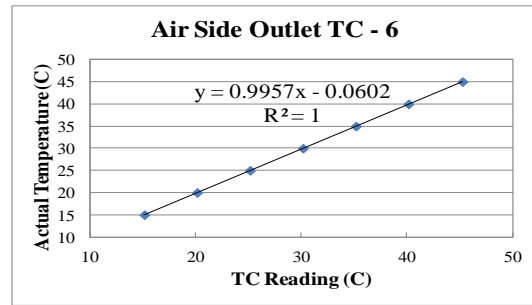
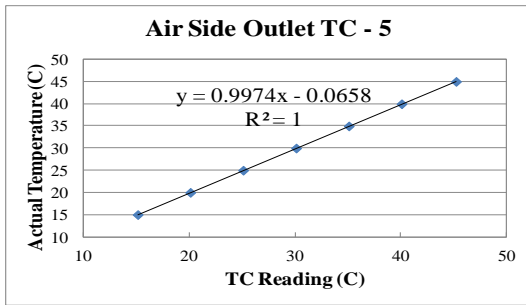
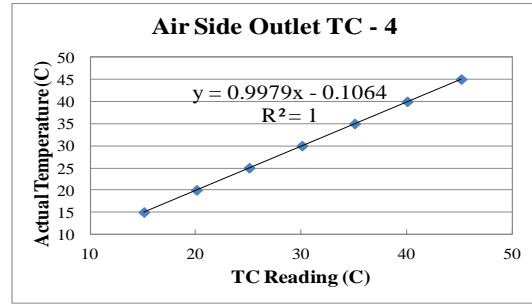
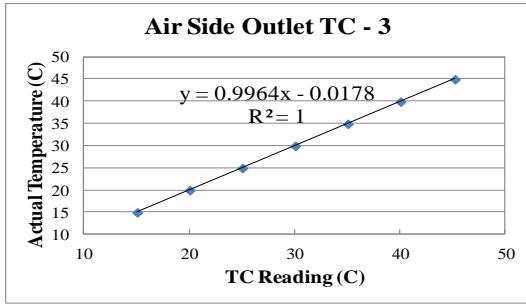
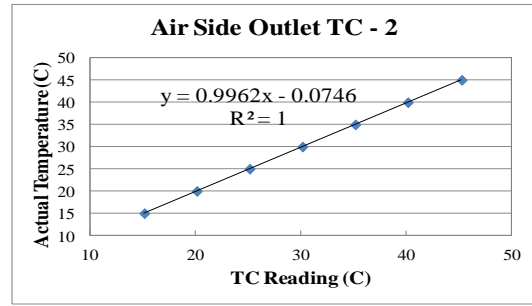
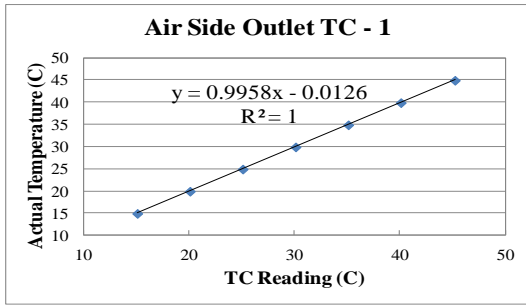


Figure 53: Air Side Outlet Thermocouples Calibration

6.2 Baseline Test Matrix

The background, design, construction, and facility calibration were completely demonstrated. The next stage of this project was moving forward to testing. The purpose of the baseline test was to establish a database of the basic, fundamental and comparable results. There were two critical requirements of the baseline, the first being that the energy balance of every case should be below 5%, otherwise the results of the baseline testing would not be reliable. Second, the inlet conditions of each test should be maintained at a constant and reasonable level or the results would not be comparable.

The expected outcomes included establishing the capacity of the tested heat exchanger and the air side pressure drop. Additional expectations included the investigation of heat exchanger capacity improvement and incremental drops in air side pressure by applying the wetting water cooling method.

Table 12 shows the test matrix for the baseline testing. It was a relatively concise test matrix; however, it effectively covered the important features of the system. Varying the heat exchanger frontal air velocity could not only test the system performance under different air-flow rates, but could also validate the air nozzle calibration results. The test facility had the feature of changing the heat exchanger inclination angle, which was included and tested in the baseline test, as well. In addition, the heat

exchanger surface condition was treated as the most essential factor of this project.

Accordingly, the baseline test also took both dry and wet conditions into account. In total, there were six test data sets, the results of which are provided in the next section.

Table 12: Baseline Test Matrix

Variables	Values	Cases
Surface condition	Dry	Wet
HX frontal air velocity	1.4 m/s, 3.5 m/s	1.4 m/s
HX inclination angle	0°, 25°	0°, 25°
Number of tests	4	2
Total number of tests		6

6.3 Uncertainty Analysis

This research was conducted experimentally. Therefore, the uncertainty of the measurement should be taken into consideration in order to ensure that the experimental results are convincing. In this section, the effect of the measurement uncertainty on the heat exchanger capacity was demonstrated. The specifications of all instruments are listed in Table 13, including the manufacturer, model number, and systematic uncertainty. All instruments were connected to the National Instruments

Field Point modules, and a LabVIEW program was used to record the data and calculate the system performance in real time.

Table 13: Specifications of Instruments

Instruments	Manufacture	Model	Systematic Uncertainty
Water Flow Meter	Sponsler	SP-1	1%
Thermocouple	Omega	T-type	$\pm 0.5^{\circ}\text{C}$
Humidity Sensor	Vaisala	HMP230 SERIES	1%
Differential Pressure Sensor	Setra	Model 264	$\pm 1\%$ F.S.
RTD Sensor	Omega	P-M-1/10-1/8	$\pm 0.1^{\circ}\text{C}$

There are two major parts in the uncertainty analysis, which are systematic uncertainty and random measurement uncertainty. The summation of the systematic uncertainty and random measurement uncertainty is the total uncertainty. The systematic uncertainty is shown in Table 13, and the random measurement uncertainty was simply equal to one standard deviation of the data that was recorded over the test duration. The definition of the total uncertainty of the measured variable is defined as Equation 18.

$$u_{\text{total}} = u_{\text{sys}} + u_{\text{STD}} \quad \text{Equation 18}$$

Where u_{sys} is the systematic uncertainty and the u_{STD} is the random measurement uncertainty.

Once the uncertainty of each measured variable was obtained, the uncertainty of the

calculated variable (which was the heat exchanger capacity in this analysis) could be calculated by using the Pythagorean summation of uncertainties method (Equation 19):

$$u_X = \sqrt{\left(\frac{\partial X}{\partial v_1} \times u_1\right)^2 + \left(\frac{\partial X}{\partial v_2} \times u_2\right)^2 + \dots + \left(\frac{\partial X}{\partial v_i} \times u_i\right)^2} \quad \text{Equation 19}$$

Where:

X is the calculated variable (heat exchanger capacity in this analysis)

u_X is the uncertainty of the calculated variable X.

v_i is the measured variable.

u_i is the uncertainty of the measured variable.

Table 14 shows the typical values for uncertainties of the measured and calculated variables for both water side and air side capacities. The analysis clearly shows that the heat exchanger capacity accuracy was significantly influenced by the temperature measurement. The percentage of uncertainty of the heat exchanger inlet and outlet temperature was 45% and 52.3%, respectively, which means the accuracy of the temperature measurements had a significant effect on the heat exchanger water side capacity. Once the temperature measurements were not as accurate as those measured by the RTD sensors that were used, the total uncertainty of the heat exchanger water side capacity was increased to unacceptable levels. On the other hand, the water side capacity was not significantly affected by the water flow rate measurement. For the

air side, the air nozzle pressure drop was the most important factor for the air side capacity, with a percentage of uncertainty of more than 51%. The temperature measurements effect was also noticeable, with the grid of nine thermocouples allowing for a low total uncertainty of 0.21°C, so that the percentage of uncertainties were 27% and 22% for inlet and outlet temperature, respectively. The total uncertainty of the air side capacity was 0.13 kW, which was much smaller than the water side capacity but not negligible. The reason might be that the temperature difference between the heat exchanger inlet and outlet was very small. Therefore, even though accurate RTDs were used to measure the water temperature, the uncertainty of the water side capacity was still an important factor for the experiments and needed to be notice.

Table 14: Uncertainties at Typical Variable Values

Water Side					
Variable	Unit	Systematic Uncertainty	Random Uncertainty	Total Uncertainty	% of Uncertainty
HX Inlet Temperature	°C	0.10	0.03	0.13	45.00
HX Outlet Temperature	°C	0.10	0.04	0.14	52.30
Water Volume Flow Rate	m ³ /s	4 X 10 ⁻⁵	3 X 10 ⁻⁵	7 X 10 ⁻⁵	2.71
HX Water Side Capacity	kW	0.25	0.06	0.31	100
Air Side					
Inlet Air Temperature	°C	0.18	0.05	0.23	26.76
Outlet Air Temperature	°C	0.18	0.03	0.21	21.99
Inlet Air RH	%	0.69	0.25	0.94	0
Outlet Air RH	%	0.40	0.18	0.58	0
Air Nozzle Pressure Drop	Pa	12.44	1.92	14.36	51.25
HX Air Side Capacity	kW	0.11	0.02	0.13	100

6.4 Results and Discussions

In this project, all the data had been recorded for at least 20 minutes after the test reached steady state. The recording time interval was 10 seconds. The average of the values of the recording period was calculated to represent the heat exchanger performance for the test case. All the test results and discussions are shown in the following sections.

6.4.1 Dry Condition Test Results

The test results of all four dry cases are listed in Table 15. For dry case 1, the experiment started from the most basic case: low air flow rate, 0° heat exchanger inclination, and under dry conditions. The inlet air conditions were maintained at about 22°C and 70% RH. The corresponding outlet air conditions were 31°C and 40% RH. The capacity of the air side capacity could be simply calculated by the following equation, based on the inlet and outlet air conditions:

$$q_a = \dot{m}_a \times C_p \times (T_o - T_i) \quad \text{Equation 20}$$

The air side capacity turned out to be about 2,800 W. Meanwhile, the heat exchanger air side pressure drop was 27 Pa.

Regarding the heat exchanger hot water side, the inlet water temperature was kept around 35°C and the outlet water temperature was 33°C. The water side capacity was calculated using Equation 21, based on the inlet and outlet water conditions.

$$q_w = \dot{m}_w \times (h_i - h_o) \quad \text{Equation 21}$$

The water side capacity was about 2,900 W. The energy balance between air and water side capacity was calculated to be 4.3%, which was considered acceptable. The third column shows the standard deviation of the data during the steady state recording period, which was a criterion to indicate if the test did or did not reach steady state. It clearly shows that all standard deviations were relatively small, which

represented small data fluctuation during the recording period indicative of relative stability, and that the average values of the data were reliable.

For dry case 2, which was a high air flow rate test case with the same 0° heat exchanger inclination angle. In order to make the test results comparable, all inlet conditions of both air and water side were basically maintained the same: 22°C and 70% RH of the inlet air, 35°C of the inlet water. Based on the same equations (Equation 20 and Equation 21), the air side and water side capacities were approximately 5,300 W and 5,100 W, respectively. The energy balance between air and water side was 3%. And all standard deviations were quite small, as seen in dry case 1. The heat exchanger capacity was increased more than double, with the air velocity increased from 1.4 to 3.5 m/s. However, the air side pressure drop also surged to 132 Pa. A detailed comparison is discussed in the following section.

Dry case 3 was for a low air flow rate and 25° heat exchanger inclination angle under dry conditions. The purpose was to investigate any differences or improvements from 0° to 25° . Except the inclination angle of the heat exchanger, all other parameters remained the same, including the inlet water temperature, inlet RH value and the temperature of the air. However, based on the same equations, Equation 20 and Equation 21, the air and water side capacity and air side pressure drop had changed slightly to 2,900 W, 2,950 W and 29 Pa, respectively. There was no significant

improvement or difference between dry case 1 and 3, even though the heat exchanger inclination angle changed from 0° to 25° . In addition, the energy balance in this dry case 3 was 2%, which was quite desirable.

The test results of dry case 4 can also be seen in this table. This test case was for a high air-flow rate and a high heat exchanger inclination angle under dry conditions.

The inlet conditions were kept the same as in dry case 3, with the exception of increasing the frontal air velocity to 3.5 m/s. The resulting air and water side capacities increased to 5,200 W and 5,100 W, respectively. Meanwhile, the air side pressure drop increased to 137 Pa. Nevertheless, when compared to dry case 2, the difference between two different inclination angles cases was insignificant. The same phenomenon occurred in the comparison between dry case 1 and 3. These results imply that the heat exchanger inclination angle does not affect the performance of a heat exchanger.

Table 15: Test Result of Dry Cases

Case Number	Dry Case 1	Dry Case 2	Dry Case 3	Dry Case 4
Surface Condition	Dry	Dry	Dry	Dry
HX Inclination Angle	0°	0°	25°	25°
Air Parameters				
Parameter	Avg. Value (Std. Dev.)	Avg. Value (Std. Dev.)	Avg. Value (Std. Dev.)	Avg. Value (Std. Dev.)
Air Velocity	1.410 (0.001)	3.524 (0.003)	1.405 (0.006)	3.464 (0.003)
Inlet Humidity (%)	68.61 (0.25)	69.19 (0.29)	70.63 (0.30)	71.18 (0.41)
Inlet Temperature (°C)	21.6 (0.05)	22.01 (0.02)	21.63 (0.02)	22.21 (0.02)
Outlet Humidity (%)	40.12 (0.18)	45.11 (0.22)	39.91 (0.19)	46.47 (0.23)
Outlet Temperature (°C)	31.02 (0.03)	29.28 (0.01)	31.53 (0.06)	29.35 (0.01)
Flow Rate (m ³ /s)	0.250 (0.001)	0.630 (0.003)	0.250 (0.001)	0.623 (0.003)
Pressure Drop (Pa)	27.28 (0.50)	132.44 (1.34)	28.87 (0.45)	137.10 (1.41)
Air Side Capacity (W)	2,763.81 (19.86)	5,275.32 (44.80)	2,889.16 (24.76)	5,168.39 (30.76)
HX Water Parameters				
Inlet Temperature (°C)	34.82 (0.03)	35.15 (0.02)	35.07 (0.13)	34.93 (0.03)
Outlet Temperature (°C)	33.04 (0.04)	31.98 (0.02)	33.29 (0.11)	31.74 (0.02)
Flow Rate (l/s)	0.390 (0.003)	0.390 (0.002)	0.399 (0.002)	0.385 (0.005)
Water Side Capacity (W)	2,887.40 (60.43)	5,121.43 (53.96)	2,949.83 (82.29)	5,103.88 (72.91)
Energy Balance (%)	4.28	3.00	2.06	1.26

6.4.2 Wet Condition Test Results

This project was designed to investigate the wetting water effect on the heat exchanger performance. Two wet condition tests were conducted at the project sponsor's suggested frontal air velocity of 1.4 m/s. By applying the wetting water method, which was described previously, the hybrid-cooled cases were tested, and the results are including in this section.

The test results of wet cases are shown in Table 16. There were three sides involved, all of which should be considered into energy balance: air, hot water, and the wetting water side. The air side, wetting water side and hot water side equations are shown below:

$$q_a = (m_a + m_v) \times h_{oa} - m_a \times h_{ia} \quad \text{Equation 22}$$

$$q_{ww} = (m_{ww} - m_v) \times h_{oww} - m_{ww} \times h_{iww} \quad \text{Equation 23}$$

$$q_w = m_w \times (h_i - h_o) \quad \text{Equation 24}$$

The energy balance was defined as:

$$\eta = \{[q_w - (q_a + q_{ww})]/q_w\} \times 100\% \quad \text{Equation 25}$$

These equations combine energy and mass balance equations. Because latent heat transfer was involved in the energy balance, the mass amount of air and wetting water was not constant. Certain amount of wetting water evaporated into the air and the air capacity was increased because the latent heat was added to the air. Therefore, if it

was assumed that a control volume enclosed the heat exchanger, then the air side capacity and the amount of the wetting water sensible heat (energy out) should be equal to the hot water side capacity (energy in).

For wet case 1, with an 0° heat exchanger inclination angle, the air side capacity was 4,600 W and the wetting water sensible capacity was 2,700 W. The heat exchanger capacity (hot water side capacity) was 7,600 W. This resulted in an energy balance of 4.2%. The capacity was greatly improved compared to dry case 1, which confirmed the expectations. The wetting water provided the potential for increasing the capacity; however, the air side pressure drop was also affected, potentially due to the wetting water blocking the fin spacing of the heat exchanger. The resulting air side pressure drop was 64 Pa. In addition, the standard deviations were also shown in this table to indicate that the data was recorded during steady state conditions.

The last case was wet case 2, with a 25° inclination angle. All the inlet conditions were identical to wet case 1. This case showed that the heat exchanger capacity was 8,300 W. The air side and wetting water side capacities were 4,500 W and 3,800 W, respectively, with an energy balance of 0.7%. In contrast to the inclination angle effect on the dry cases, the capacity of the wet case was increased with the increased inclination angle, changing from 7,600 W to 8,300 W. But the effect of the inclination angle on the air side pressure drop was not remarkable, varying from 64 to 66 Pa.

Table 16: Test Result of Wet Cases

Case Number	Wet Case 1	Wet Case 2
Surface Condition	Wet	Wet
HX Inclination Angle	0°	25°
Air Parameters		
Parameter	Avg. Value (Std. Dev.)	Avg. Value (Std. Dev.)
Air Velocity (m/s)	1.41 (0.01)	1.41 (0.01)
Inlet Humidity (%)	77.19 (0.13)	73.01 (0.19)
Inlet Temperature (°C)	21.51 (0.03)	21.51 (0.03)
Outlet Humidity (%)	72.00 (0.25)	63.55 (0.42)
Outlet Temperature (°C)	27.18 (0.02)	28.04 (0.03)
Flow Rate (m ³ /s)	0.253 (0.001)	0.253 (0.001)
HX Pressure Drop (Pa)	64.00 (1.29)	66.57 (1.12)
Air Side Capacity (W)	4,606.96 (36.95)	4,476.37 (45.62)
HX Water Parameters		
Inlet Temperature (°C)	34.97 (0.03)	34.9 (0.02)
Outlet Temperature (°C)	30.19 (0.02)	29.72 (0.02)
Flow Rate (l/s)	0.385 (0.002)	0.385 (0.002)
Water Side Capacity (W)	7,642.02 (50.03)	8,290.93 (112.10)
Wetting Water Parameters		
Inlet temperature (°C)	22.51 (0.02)	22.32 (0.02)
Outlet temperature (°C)	26.38 (0.02)	27.81 (0.06)
Flow rate (l/s)	0.168 (0.008)	0.164 (0.004)
Sensible heat (W)	2,712.53 (127.44)	3,757.46 (106.98)
Energy Balance (%)	4.2	0.69

6.4.3 Comparisons and Discussions

Figure 54 shows the overall heat exchanger capacity comparison. It can be seen clearly that the heat exchanger capacity varied with different test conditions. Dry cases 1 and 2 showed the lowest capacity. This was reasonable due to the low air-flow rate and dry conditions, which offered no advantage from latent heat transfer. The capacities of these two dry cases were each less than 3 kW. Moreover, once the heat exchanger frontal air velocity was increased to 3.5 m/s, the capacities of the heat exchanger were also significantly increasing, to more than 5,000 W. The capacity increments were 77% and 73% for 0° and 25° inclination angles, respectively. These improvements came from the increased air-flow rate, and the improved ability to dissipate heat from the heat exchanger surface via convective heat transfer. However, the heat exchanger inclination angle effect on the capacity was not remarkable. This chart shows that there was little difference between inclination angle cases for each air velocity. The heat exchanger capacity differences were only 2.2% and 0.3% for low air-flow rate and high air-flow rate conditions, respectively. This might be because even though the heat exchanger inclination angle changed, the other geometry parameters of the heat exchanger still remained the same. Further, the frontal area of the heat exchanger was also unchanged; therefore, the frontal air velocity should not change either. Based on the above reasons, most of the important factors of heat

exchanger capacity were identical. Accordingly, it was reasonable that the capacities remained unchanged for each air velocity case.

The hybrid cooling method was applied for both wet cases 1 and 2. Because of the latent heat transfer advantage, a significant capacity improvement could be seen from dry cases 1 and 2 to wet cases 1 and 2. The improvements were 174% and 181% for 0 and 25°, respectively. These noticeable capacity improvements were the expected outcome from the hybrid cooling method. Applying the wetting water allowed the heat exchanger capacity to take advantage of both the sensible and latent heat transfer.

The latent heat was added to the air capacity from the previous tables (Table 15 and Table 16), and it could be seen that the air side capacity had essential increments of roughly 56%. Furthermore, the extra sensible heat was also taken into account. The amount of wetting water sensible heat increment was more than 2,700 W. Based on the above analysis, the heat exchanger capacities increased to more than 7,600 W.

However, under wet conditions, the heat exchanger capacity was more sensitive to the inclination angle than it was under dry conditions. The capacity rose by 8.5% from the 0° case to the 25° case. This behavior is significantly different from the behavior of the dry cases. This phenomenon might be attributable to the water distribution on the fins of the heat exchanger. Although it was not easy to observe the wetting water flow pattern on the heat exchanger fins, the water distribution was still considered to be an

important reason for the capacity increase. It was speculated that due to the inclination of the heat exchanger, the wetting water might be able to cover more of the surface area of the heat exchanger fins. Accordingly, this would provide a greater heat transfer area, thus more heat dissipation and a higher heat exchanger capacity.

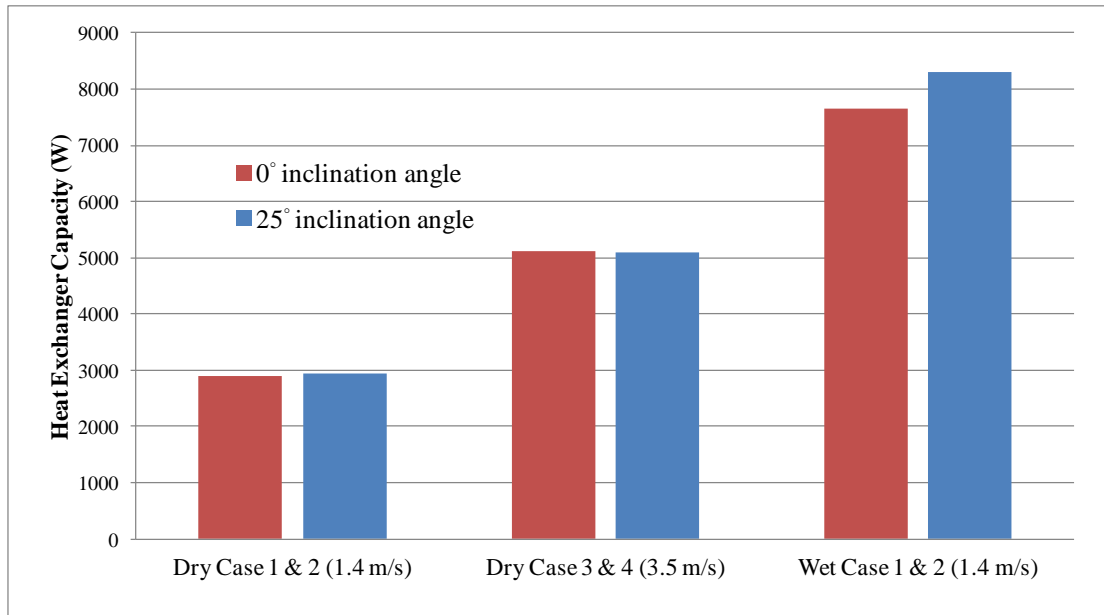


Figure 54: Overall Heat Exchanger Capacity Comparison

The other important heat exchanger performance index was the air side pressure drop. The reason for considering the heat exchanger air side pressure drop was related to the size of the air fan. From the economic point of view, a larger air side pressure drop requires a larger air fan to provide sufficient air-flow rate; a larger air fan means a higher investment and operating costs, and potentially more operating noise. Figure 55 shows the air side pressure drop for each test condition. This shows that the air side pressure drop was more sensitive to the air velocity than the surface condition.

Dry cases 1 and 2 had the lowest air side pressure from about 27 to 29 Pa; however, once the frontal air velocity increased to 3.5 m/s, the air side pressure drop surged over 130 Pa. For the wet condition cases, because the fin spacing of the tested heat exchanger was not optimized, the wetting water might have blocked the heat exchanger frontal free area (space between fins). This led to the air side pressure drop being much higher than the dry case at the same air velocity. Respectively, the air side pressure drop was increased by 135% and 131% for the 0° and 25° cases, respectively

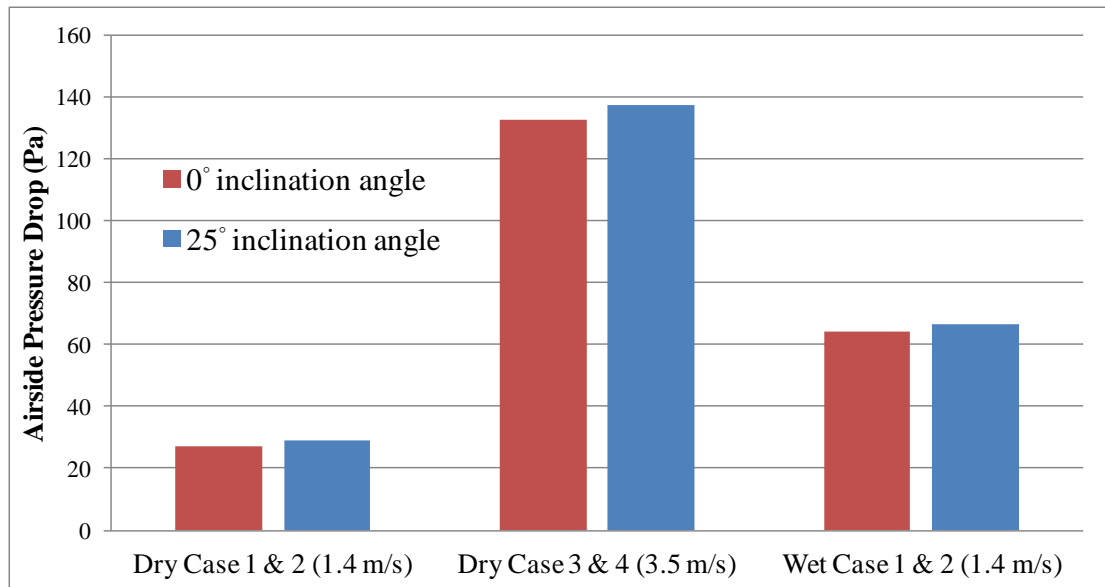


Figure 55: Overall Air Side Pressure Drop Comparison

Figure 56 shows the air fan pumping power for each case. The pumping power calculation was based on the following equation:

$$P = \Delta p \times v \times A$$

Equation 26

Where Δp is the air side pressure drop, v is the heat exchanger frontal air velocity, and A is the heat exchanger frontal area.

At a higher frontal air velocity, it can be seen that the air fan pumping power increased because it was the function of both pressure drop and air velocity. This chart shows that pumping power was only about 7 W for the low air-flow rate dry cases, and the pumping power increased to 16~17 W for low air-flow rate wet cases. However, it consumed more than 80 W of power to overcome the significant pressure drop associated with high air velocity.

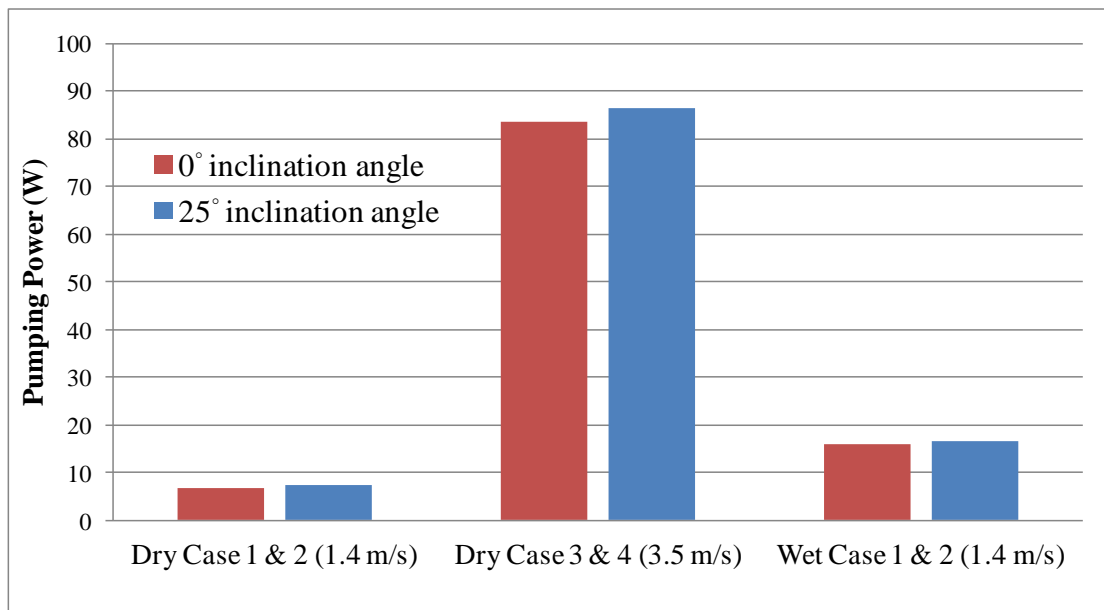


Figure 56: Overall Air Fan Pumping Power Comparison

In summary, even though the higher air-flow rate could increase the heat exchanger capacity without any extra wetting water system, a much larger air fan might be required to achieve the expected performance. On the other hand, a hybrid cooling

method has the potential to improve the heat exchanger capacity, without requiring an over-sized air fan to overcome the extra pressure drop that comes from the wetting water.

7. Summary and Conclusions

A test system was designed and constructed to measure the performance of an air-cooled heat exchanger under dry and wet conditions. The system was designed and sized for a 17 kW heat exchanger. The tested heat exchanger simulated a commercial condenser. Hot water was used as the working fluid. There were three fluid streams involved in this test system: air side, heat exchanger hot water side, and wetting water side. For the air side, a test section and wind tunnel were designed and built. All the components and instrumentation were sized and mounted based on the ASHRAE Standard 41.2 [15]. Regarding the heat exchanger hot water side, all instrumentation was appropriately sized and installed. The water volume flow rate and water temperatures were measured to calculate the heat exchanger capacity. Additionally, instead of using an electrical water heater, a heat pump was built to provide the heat to the hot water side; hence, the components of this heat pump were sized and mounted appropriately. For the wetting water side, a water chiller was used to maintain the wetting water temperature, and the water volume flow rate and the temperatures were also measured. Moreover, the wetting water feeding and draining system were also built to re-circulate the wetting water.

In order to obtain accurate test results, the instruments were accurately calibrated, including the air nozzles, water turbine flow meters, relative humidity sensors, and air

side thermocouple grids.

The baseline tests were conducted with a fin and tube heat exchanger. The baseline tests were divided into two main categories: dry and wet conditions. To investigate the heat exchanger performance under different test conditions, the entire test matrix included six tests. Four of them were under dry conditions and two were under wet conditions. Different heat exchanger frontal air velocity and heat exchanger inclination angles were tested. Frontal air velocity varied from 1.4 m/s to 3.5 m/s, and the heat exchanger inclination angles were changed from 0° to 25°.

In this project, only steady-state results were recorded and discussed. The results showed that the heat exchanger with a dry surface at a low air-flow rate had the lowest capacity of about 3 kW. When the air velocity increased to 3.5 m/s, the capacity also increased to more than 5 kW. This capacity increment shows that the heat exchanger was very sensitive to the frontal air velocity. However, changing the heat exchanger inclination angle did not significantly affect the performance of the heat exchanger. This might be because most of the geometrical parameters of the heat exchanger were not changed with the inclination angle changing; however, the heat exchanger performance mostly depends on the heat exchanger geometrical parameters when other working conditions were maintained identically. Accordingly, the capacity of the heat exchanger was not sensitive to the inclination angle. The capacity changed

only 2.2% and 0.3% for low and high air-flow rate cases.

When the hybrid cooling was applied, the capacity of the heat exchanger had a remarkable improvement. The results showed that the capacities improved more than 170%, no matter what the inclination angle was. This showed that the hybrid cooling method had a high potential for improving the performance of the heat exchanger even though the tested heat exchanger was not optimized yet. However, the heat exchanger capacity was sensitive to the inclination angle under wet conditions. The capacity increased by 8.5% when the inclination angle varied from 0° to 25°. The speculative reason was the water distribution on the fin surface.

Another outcome of this project was the investigation of the heat exchanger air side pressure drop. As was expected, the heat exchanger had the lowest air side pressure drop of nearly 30 Pa at low air velocity under dry surface conditions, and significantly increased to higher than 130 Pa at high air velocity. Additionally, the air side pressure drop also increased due to the water blockage between the heat exchanger fins under wet conditions. It increased to more than 64 Pa, which was much lower than it was at high air velocity under dry conditions. Furthermore, the air fan pumping power was highly related to the heat exchanger air side pressure drop. The higher air side pressure drop led to greater power consumption in the form of a larger air fan, and most likely, increased both operating costs and noise. Therefore, the relationship

between the heat exchanger air side pressure drop and the required air fan pumping power was analyzed. Due to the fact that the pumping power was a function of both pressure drop and air-flow velocity, the power consumption of the cases at high air flow rates under dry conditions was more than 80 W when it was only about 7 W at low air velocity and 17 W under wet conditions.

Overall, the steady state baseline test results of a round-tube-fin heat exchanger showed that the heat exchanger performance was sensitive to the frontal air velocity and heat exchanger surface condition. However, the heat exchanger inclination angle was not an important factor with respect to both the heat exchanger capacity and air side pressure drop, except for the capacity under wet conditions. The heat exchanger capacity was increased with the frontal air velocity and surged even more by applying a hybrid cooling method. Meanwhile, the air side pressure drop and the air fan pumping power consumption were also investigated. The results showed that they were more sensitive to the air velocity than the surface conditions.

8. Recommendations and Future Work

For future experimental research, it is recommended that the geometry of the heat exchanger could be optimized in order to obtain the optimized performance of capacity and air side pressure drop by applying hybrid cooling methods. Additionally, by using CFD software, such as Fluent, the water distribution behavior could be simulated. A better understanding of the proper water distribution could help the optimization of the heat exchanger.

For the testing conditions, it is recommended that the water flow rate could also be taken into consideration. Due to the fact that the performance was very sensitive to the surface conditions (dry or wet), the wetting water flow rate and the amount of the wetting water might be an essential factor of the heat exchanger performance under wet conditions. In addition, the heat exchanger performance would also be affected by the surface wettability [22, 23]. Therefore, the heat exchanger surface treatment might be another potential research target.

To be more realistic, the tested heat exchanger in this project is supposed to be a part of outdoor HVAC unit, hence, different climate situations could occur. Mixtures of various fractions of water and glycol might be used as the working fluid for wetting water and heat exchanger hot water in order to allow the heat exchanger to also work in ambient temperatures lower than the freezing point of water.

References:

- [1] Min and Webb, 2001, *Condensate formation and drainage on typical fin materials*, Experimental Thermal Fluid Sciences, Vol.25, pp. 101-111.
- [2] Yang and Clark, 1974, *Spray Cooling of Air-Cooled Compact Heat Exchangers*, Int. J. Heat Mass Transfer Vol.18 pp. 311-317.
- [3] Leidenfrost and Korenic, 1979, *Analysis of Evaporative Cooling and Enhancement of Condenser Efficiency and of Coefficient of Performance*, Wärme- und Stoffübertragung Vol. 12, pp. 5-23.
- [4] Song, Lee and Ro, 2003, *Cooling enhancement in an air-cooled finned heat exchanger by thin water film evaporation*, Int. J. Heat Mass Transfer Vol.46 pp. 1241-1249.
- [5] Wang, Lee, Sheu and Chang, 2001, *A comparison of the airside performance of the fin-and –tube heat exchangers in wet condition; with and without hydrophilic coating*, Applied Thermal Engineering Vol.22, pp. 267-278.
- [6] Wang, Lin and Lee, 1999, *Heat and momentum transfer for compact louvered fin-and-tube heat exchangers in wet conditions*, Int. J. Heat Mass Transfer Vol.43 pp. 3443-3452.
- [7] Kim, Lee, Mehendale and Webb, 2003, *Microchannel Heat Exchanger Design for Evaporator and Condenser Applications*, Advances in Heat Transfer, Vol. 37, pp. 297-435.
- [8] Kim and Bullard, 2000, *Air-side thermal hydraulic performance of multi-louvered fin aluminum heat exchangers*, Int. J. Refrigeration, Vol.25, pp. 390-400.
- [9] Kim and Bullard, 2002, *Air-side performance of brazed aluminum heat exchangers under dehumidifying conditions*, Intl. J. Refrigeration, Vol.25, pp. 924-934.
- [10] Park and Jacobi, 2009, *Air-side heat transfer and friction correlations for flat-tube louver-fin heat exchangers*, J. Heat Transfer, Vol. 131, pp. 021801-1- 061801-12.
- [11] Park and Jacobi, 2009, *The air-side thermal-hydraulic performance of flat-tube heat exchangers with louvered, wavy, and plain fins under dry and wet conditions*, J. Heat Transfer, Vol. 131, pp. 061801-1- 061801-13.
- [12] Chang and Wang, 1996, *A generalized heat transfer correlation for louver fin geometry*, Int. J. Heat Mass Transfer Vol.40, pp. 533-544.
- [13] Silk, Kim and Kiger, 2006, *Spray cooling of enhanced surfaces: Impact of structured surface geometry and spray axis inclination*, Intl. J. Heat Mass

- Transfer, Vol.49, pp. 4910-4920.
- [14] Coursey, Kim and Kiger, 2007, *Spray Cooling of High Aspect Ratio Open Microchannel*, J. Heat Transfer, Vol. 129, pp. 1052-1059.
- [15] ASHRAE Standard 41.2 1987, *Standard Methods for Laboratory Airflow Measurement*.
- [16] Moody, 1944, *Friction factors for pipe flow*, Transactions of the ASME 66 (8): pp. 671–684.
- [17] *Oberdorfer Pump F13-600 Performance Curve*
< http://www.pumpvendor.com/media/oberdorfer/pdf/600_series.pdf>.
- [18] Price Pump Company, *HP75SS Pump Performance Curve*.
- [19] Copeland, Emerson Climate Technologies *Compressor Performance Information*, < <http://www.emersonclimate.com/en-US/Pages/home.aspx>>.
- [20] Swagelok Technical Bulletin, 2007, *Valve Sizing*,
<<http://www.swagelok.com/downloads/webcatalogs/EN/MS-06-84.PDF>>.
- [21] Greenspan, 1977, *Humidity Fixed Points of Binary Saturated Aqueous Solutions*, J. Research of the National Bureau of Standards, Vol.81A, pp. 89-96.
- [22] Sugawara and Itaru, 1956, *Researches on the Heat Transfer by Dropwise Condensation*, Memoris Faculty of Energ., Kyoto Univ. Vol.18, pp. 84-111.
- [23] Min, Peng and Wang, 2002, *Departure Diameter of a Drop on a Vertical Plate*, J. Basic Science Engineering, Vol. 10, pp. 57-62.